



National Technical University of Athens  
School of Naval Architecture and Marine Engineering  
Division of Marine Structures  
Shipbuilding Technology Laboratory

Diploma Thesis

**Damage Identification in Simplified Geometries Utilising  
Machine Learning Methods: A Computational Study**

Anastasios Katsoudas

Thesis Supervisor: Konstantinos N. Anyfantis, Assistant Professor

ATHENS, JULY 2022

## **Acknowledgements**

This work is the final assignment for the completion of my studies at the School of Naval Architecture and Marine Engineering. These academic years have been pivotal in shaping both my personal and professional trajectory. I leave this school grateful for everything I learned, the moments I experienced, the friends I made and the people I met.

I would like to express my gratitude towards my thesis supervisor, Assistant Professor Konstantinos Anyfantis. His passion for the topic and ability to share knowledge in lectures captured my interest and inspired me to get involved in structural engineering. His guidance and immediate support throughout this work were invaluable. For all the above I am grateful.

I would like to thank the members of my supervisory committee, Professor Nicholas Tsouvalis and Professor Lambros Kaiktsis, offering their scientific expertise for the evaluation of my thesis.

I would also like to thank Ph.D. candidate Nikolaos Silionis for his enormous contribution. His will to share ideas and his prompt support in overcoming day-to-day obstacles were crucial in the preparation of this work.

Finally, I owe my deepest gratitude to my family for their unconditional love and endless support throughout my life. Also, I am sincerely grateful to my friends for making every ordinary day special.

Anastasios Katsoudas

Athens, 2022

## Περίληψη

Οι ναυπηγικές κατασκευές λειτουργούν σε εξαιρετικά διαβρωτικό περιβάλλον και η τρέχουσα πρακτική της βιομηχανίας είναι να λαμβάνεται υπόψη κατά τη σχεδίαση η απώλεια πάχους λόγω διάβρωσης. Επίσης, αντικαθίστανται προληπτικά τμήματα της κατασκευής που μετρούνται εκτός ορισμένων ορίων κατά τους τακτικούς ελέγχους. Επομένως, ο εντοπισμός βλαβών και η αξιολόγηση της κατάστασης της κατασκευής γίνονται σε προδιαγεγραμμένο χρονοδιάγραμμα. Γίνεται κατανοητό ότι θα υπάρχουν άμεσα πλεονεκτήματα από την εφαρμογή ενός συστήματος παρακολούθησης υγείας των κατασκευών, το οποίο θα επέτρεπε τη μετάβαση σε τακτικές συντήρησης με βάση την τρέχουσα κατάσταση τους.

Ο στόχος της παρούσας μελέτης είναι να διερευνηθούν και να αξιολογηθούν ορισμένες μέθοδοι από την Στατιστική Αναγνώριση Προτύπων και τη Μηχανική Εκμάθηση, στην ικανότητα εντοπισμού απώλειας πάχους με βάση μετρήσεις παραμορφώσεων. Για το σκοπό αυτό θεωρήθηκε μια ορθογωνική πλάκα με διάφορα επίπεδα γενικευμένης και εντοπισμένης απώλειας πάχους, η οποία υπόκειται σε ένα φορτίο πίεσης μοντελοποιημένο υπό στοχαστική θεώρηση. Η απόκριση της πλάκας προσομοιώθηκε σε περιβάλλον πεπερασμένων στοιχείων από όπου προέκυψαν μετρήσεις παραμορφώσεων. Τα δεδομένα παραμορφώσεων χρησιμοποιήθηκαν για την μοντελοποίηση και την αξιολόγηση των προαναφερθέντων μεθόδων.

## **Abstract**

In the highly corrosive environment where marine structures operate, the current industry practice is to overcompensate for corrosion induced thickness loss (CITL) and replace any parts that score below specified allowable limits during scheduled maintenance. Damage detection and evaluation are conducted on a planned maintenance scheme. Hence, there would be immediate benefits from the implementation of a structural health monitoring (SHM) system that would allow for predictive, condition-based maintenance.

The objective of this study is to investigate and assess the effectiveness of state-of-the-art statistical pattern recognition (SPR) and machine learning (ML) methods in association with alternative sensor grid architectures as a SHM scheme for the detection of CITL. For this purpose, a simple rectangular plate at different corrosion levels (uniform and pitting) was considered as a reference structural element, which was subjected to a stochastic pressure load. Strain response data were produced using Finite Element (FE) simulations and were treated under a probabilistic framework. Elements from detection theory and ML were taken under consideration in order to construct alternative detectors and assess their performance.

# Table of Contents

Abbreviations .....	7
1 Introduction.....	1
1.1 Current State of Damage Identification Practices .....	1
1.2 Structural Health Monitoring .....	4
1.3 Thesis Objectives and Overview .....	8
2 Theoretical Background.....	12
2.1 Statistical Pattern Recognition (SPR) .....	12
2.1.1 Likelihood Ratio Test (LRT) .....	13
2.1.2 Discordant Outlier Analysis.....	14
2.1.3 Quadratic Discriminant Analysis (QDA).....	15
2.2 Principal Components Analysis .....	18
2.3 Artificial Neural Networks (ANNs).....	19
2.3.1 Introduction to Artificial Intelligence, Machine Learning and ANNs.....	19
2.3.2 Artificial Neuron Modeling .....	21
2.3.3 Activation Functions.....	22
2.3.4 ANN Training Process .....	25
2.3.5 Summary .....	27
2.4 Fundamentals of Finite Element Analysis (FEA) .....	28
2.4.1 Basic Principles of the Finite Element Method .....	28
2.4.2 FE Modeling of Thin-walled Structures .....	34
2.4.3 Summary .....	36
3 Problem Definition.....	37
3.1 Idealised Plate Domain.....	37
3.2 Operational Variability Definition .....	38

3.3	Sensor topology.....	41
3.4	Damage introduction.....	42
3.5	Finite Element Modeling.....	44
4	Exploratory Data Analysis.....	48
4.1	Dataset Construction.....	48
4.2	Data Preprocessing.....	50
4.2.1	Statistical Patterns of the Strain Response.....	50
4.2.2	PCA of the Input Vectors.....	55
5	Results and discussion.....	58
5.1	Formulation of the Detectors.....	58
5.1.1	Likelihood Ratio Test.....	59
5.1.2	Discordant Outlier Analysis.....	59
5.1.3	Quadratic Discriminant Analysis.....	60
5.2	Detection metrics.....	60
5.3	Detection of uniform corrosion.....	61
5.4	Detection of localised corrosion.....	64
6	Concluding Remarks.....	68
6.1	General Remarks and Future Research.....	68
7	Appendix.....	69
7.1	List of Figures.....	69
8	References.....	72

## Abbreviations

Artificial Intelligence	AI
Artificial Neural Network	ANN
Common Structural Rules	CSR
Cumulative Distribution Function	CDF
Degrees of Freedom	DOFs
Digital Twin	DT
False Alarm Rate	FAR
International Association of Classification Societies	IACS
International Maritime Organization	IMO
inverse Finite Element Method	iFEM
Latin Hypercube Sampling	LHS
Likelihood Ratio Test	LRT
Linear / Quadratic Discriminant Analysis	LDA/QDA
Machine Learning	ML
Monte Carlo Simulation	MCS
Non-Destructive Evaluation / Testing	NDE/NDT
Principal Component Analysis	PCA
Principal Components	PCs
Probability Density Function	PDF
Probability of Detection	POD
Singular Value Decomposition	SVD
Statistical Pattern Recognition	SPR
Stochastic Gradient Descent	SGD
Structural Health Monitoring	SHM

# 1 Introduction

## 1.1 Current State of Damage Identification Practices

At the heart of structural engineering lies the notion of safe design. The most common and effective practices to ensure the safe operation of a structure have remained unchanged over the better part of modern engineering history. These practices essentially are: a) significantly overcompensating for vaguely defined potential loading scenarios, usually of stochastic nature as well as uncertainty regarding the material, and b) planning ahead for normal wear. This is especially the case in the highly unpredictable and corrosive environment where naval vessels and marine structures operate. In addition to conservative design, periodical surveys and maintenance are required throughout the life cycle of a structure. In the maritime industry current practices involve strict preventive maintenance schemes centered around temporally fixed inspections that are imposed by the International Maritime Organization (IMO) and overseen by classification societies. Damage identification is based on visual inspection and non-destructive evaluation (NDE) carried out on site in predetermined minimum time intervals. Due to the vast number of structural elements a ship is composed of, surveys focus on designated areas and structural details that are expected to be corroded or are susceptible to certain types of failure [1].

In Figure 1 the sketch of a transverse section of a typical dry cargo vessel is depicted. Marked on it are notes and comments regarding damage modes most frequently occurring on each of the designated locations. This figure is provided in a relevant report of recommendations regarding the inspection of bulk carriers and tankers, published by the International Association of Classification Societies (IACS) and is presented here as an illustration of the procedures discussed above.



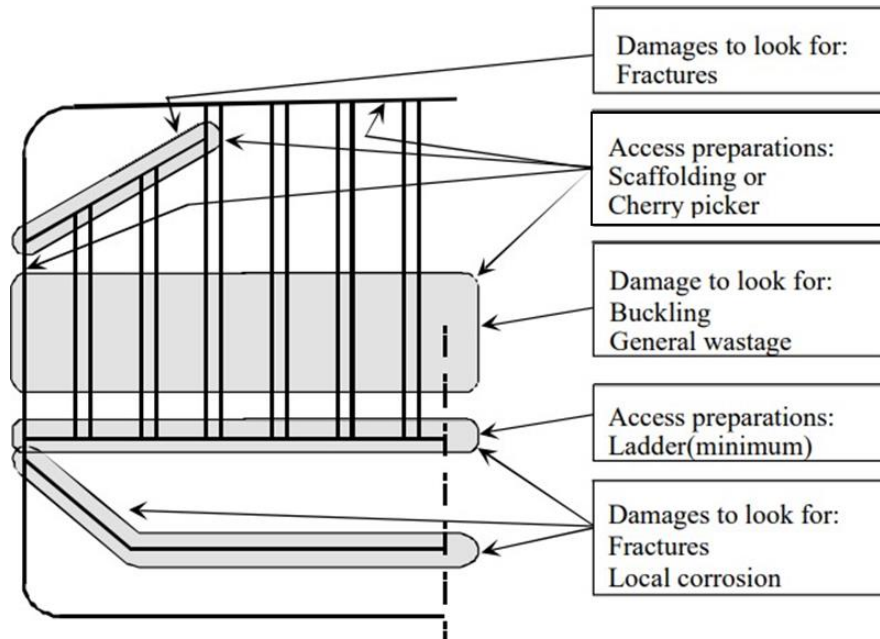


Figure 1. Sketch of traverse bulkhead with instructions for damage inspection as recommended by IACS guidelines (Source: IACS [1]).

This methodology of plan-based inspections, although effective, is costly and inefficient. It requires sacrifice of operational time and waste of resources (materials and man-hours). It is also a cause of marine pollution and requires work in a hazardous environment. The aforementioned drawbacks could be mitigated with the implementation of an alternative, condition-based maintenance system.

In the marine operational environment, one of the prevalent types of damage is corrosion induced thickness loss (CITL). This type of damage is part of the normal operational wear of marine structures for which structural guidelines [2] require the addition of excess thickness to structural members. Common modes of corrosion involve uniform corrosion of extensive areas as well as pitting. Pitting is a type of localised corrosion that takes the form of small craters of variable size and geometry on the material. Usually, those craters are concentrated around specific locations forming a damaged area resembling locally contained uniform corrosion [3]. This mode of corrosion, along with uniform thickness loss is prevalent on plates in the marine environment. Typically, the material addition to plates required by guidelines [2] for safe design against corrosion constitutes 20% of the nominal plate thickness. The nominal thickness is also dictated by the guidelines to ensure safe operation under expected loading conditions during the lifespan of the structure.

Currently, for the evaluation of the condition of ships and offshore structures, the main inspection methods used are: visual inspection, radiography, ultrasonic testing and magnetic particle or liquid penetrant testing [4]. Since the majority of marine vessels and offshore structures are mainly constructed of metal, in the present study it is implied that the subject material of reference is metal without any explicit mention further on.

Visual inspection is the simplest form of condition evaluation. Rust accumulation, unexpected buckling patterns or plastic deformation, craters due to corrosion are strong visual evidence of fault locations. Although damage may not always be visible to the naked eye and visual condition evaluation is very limited, visual inspection can detect useful hints about potential flaw locations. In these locations, later on, more sophisticated methods can be targeted, hence visual inspection is an important starting stage for surveys.

Radiography testing is very closely related to quality control and inspection of weld joints. It is known that welds, by design, are susceptible to internal defects such as enclosed gas bubbles, weld material contaminants, internal cracking and other discontinuities which can be found deep below the surface. Radiography can provide better insight in the internal condition of weld joints, allowing for accurate identification and characterisation of the aforementioned defects. In light of this information, the condition of the weld can be assessed, leading to informed decision making. On the downside, the equipment required for radiography is expensive, is not always portable and poses serious health hazard for human operators.

Similarly, magnetic particle and liquid penetrant testing are implemented to visualise and locate surface cracking, usually on plates or joints. For these inspection methods, less sophisticated equipment is required, such as spray-on indicator substances and a magnetic probe at most, which is easily portable on site and less dangerous to operators. A drawback of these methods is the limitation to near surface defects. While pitting corrosion, when at an advanced stage, makes distinct patterns on surfaces visible to the naked eye, this method of chemical testing can detect the initial formation of craters early on when they are still not visible. Although, in that early stage, this defect does not pose a structural risk, detecting areas of formation can assist in preventing the propagation and deterioration of the problem.

Regarding uniform thickness loss due to corrosion, on which the present work focuses as well, ultrasonic testing is mainly used. In this inspection method, ultrasound probes are used to measure

plate thickness. The required equipment is fairly portable and safe to operators. Common procedures require painstakingly sampling plate thickness measurements across large areas to paint a picture of the overall shell condition. In areas around measurements where excessive loss is indicated, the sample count is explicitly increased.

The aforementioned NDE methods have many drawbacks. Firstly, human intervention is required. On top of that, the inspector is required to be highly skilled with great expertise and pass high qualification standards in order to ensure correct evaluation of the readings. Techniques require that the vicinity of the damage is known a priori and that the portion of the structure being inspected is readily accessible. Prevention is based in statistically locating faults by sample tests throughout the structure, focusing on areas susceptible to damage. Additionally, most methods are limited to detection of damage on or near the surface of the structure [5]. Moreover, NDE is applied on a single damage instance, at a specific timeframe. No information is gained about the evolution of the damage when operation continues or the overall health of the structure given the presence of the damage.

Furthermore, in order to transition to more environmentally and economically sustainable structures, it is required to reduce material wastage. It would be of immediate benefit to work components closer to failure rather than preventively replacing them because of uncertainty about their remaining operational reliability. This need for quantitative global damage detection and structure evaluation methods drives the development of structural health monitoring systems, as a reliable methodology to transition to condition based maintenance schemes.

## **1.2 Structural Health Monitoring**

Structural Health Monitoring (SHM) can be defined as a continuous, automatic evaluation of the state of a structure as a whole, or its individual components [6]. SHM involves the use of sensory equipment to get continuous measurements of the response of a structure. These measurements are processed appropriately to deduce a conclusion about the state of the structure. Also, the decision whether it can reliably perform its intended function based on the evaluation of the measured data is considered part of the SHM framework.

The structural response can be affected by natural factors such as ageing and degradation, while, commonly, the operation of the structure itself (e.g., decreasing fuel in a tank, or moving components) can be a factor that impacts its behaviour. Hence, in order to draw reliable conclusions, these alterations must be taken into account. It is understood that in SHM the whole procedure of measurement-processing-evaluation should be periodically updated, because the condition of the structure inevitably does not remain as designed throughout its operational life. It is made clear, that SHM should be regarded as a dynamic sub-system that accompanies the structure throughout its lifecycle [7, 8].

The SHM framework should not be considered just another NDE method. In defence of this statement, note for example the case of an extreme event that exceeds operational specifications. In such a scenario traditional NDE methods usually require cease of operations. On the contrary, a SHM system can provide immediate feedback on the condition of the structure and assist in deciding whether operations can safely continue afterwards. Another fundamental differentiation element is that in order to apply NDE techniques, the existence of damage should already be known, while damage detection falls within the scope of SHM systems. Furthermore, NDE does not provide up-to-date information on the overall state of the structure. On the other hand, SHM refers to near real-time systems that function in parallel with the operation of the structure. Such systems are, amongst other tools, a key feature in the implementation of Digital Twin (DT) practices in the industry [9].

The term Digital Twin refers to a virtual counterpart of a structure or a system. Essentially, it can be regarded as a virtual, central hub where all information regarding the system is gathered, processed and controlled. The DT mirrors its real-world counterpart throughout its life. While this framework bares much similarity with SHM as described above, it is rather a generalisation of the same principles. The DT is not limited to information concerning the structural health of a system, rather it may include data regarding operational procedures, performance metrics, financial analytics and anything of interest depending on each application. Such a framework offers a live overview of a system which renders it more manageable by the operators. Additionally, that invaluable concentration of information can be used to simulate future or alternative states of the system and make predictions offering risk-free experimental grounds to be used for optimisation of the system.

A lot of future applications for SHM can be visualised. While there are several interesting aspects of SHM, for the purposes of the present study let's remain focused in SHM as a damage-detection strategy. This idea of SHM as a damage-detection method is described by Farrar et al [5] as the following procedure:

- Step 1: Operational evaluation.
- Step 2: Data acquisition, normalisation, and cleansing.
- Step 3: Feature extraction and data condensation.
- Step 4: Statistical model development for feature discrimination.

The flowchart of Figure 2 is a great overview of the process described above.

In step 4, the model established is necessary for the evaluation of the state of the structure. According to Rytter [10], there are four levels of damage evaluation:

- Level 1: Presence identification.
- Level 2: Location determination.
- Level 3: Severity characterisation.
- Level 4: Remaining operational life prediction.

Plates on a marine vessel, which is the subject of analysis in this work, are required to be replaced once damage exceeds a threshold indicated by formal guidelines. Hence, focus is pointed towards only level 1 SHM statistical model development. It is believed that the latter model could be used for early damage detection and consequently assist in dynamic, condition-based maintenance planning according to current structural state, offering a way out of time-based maintenance schemes.

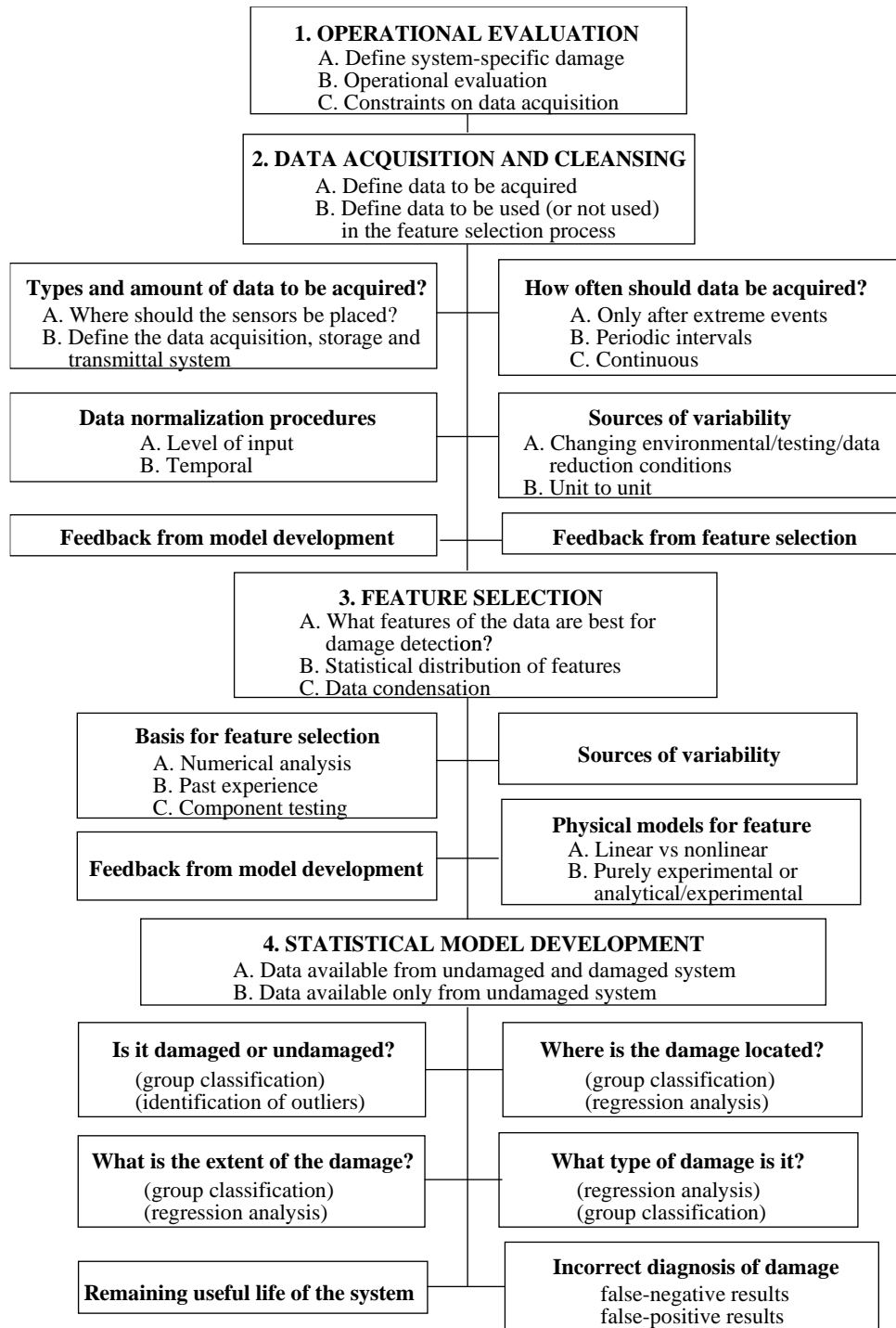


Figure 2. Flowchart overview of the processes of SHM (Source: Farrar et al [5]).

As presented in the last few paragraphs, SHM can be viewed as a problem belonging to the field of machine learning (ML) and more specifically pattern recognition, as recognised by Worden et al [7, 11]. The same view of the topic is found widely across the literature. One paradigm of this is the work of Sohn et al [12], in which fiber optic strain gauge data were obtained corresponding to two structural conditions of a boat and were submitted to two pattern recognition techniques based on time series analysis to discriminate between the structural conditions.

As is the case with the previous example, the strain response of the structure is often used as the source of information for SHM. Strain-based pattern recognition was also utilised in some of the earliest such paradigms to detect the presence, location and size of damage in stiffened panels with the use of a neural network by Kudva et al [13]. The same principle is followed in the more recent works of Anyfantis [9] and Silionis et al [14] for detection and localisation of extensive damage in thin-walled structures as well as by Liangou et al [15] for studying optimal sensor placement in relevant applications.

In the marine and offshore industry, SHM implementations are frequently discussed. Corrosion detection on ship hull structures is studied in the works by Yao et al [16], where a machine-vision, image-based approach is implemented and by Silionis et al [17] where a strain-based approach is implemented. Displacement and stress monitoring via applying a technic called inverse Finite Element Method (iFEM) on strain measurements is suggested by Kefal et al [18]. Nonetheless, to the author's knowledge, the applications of SHM systems in the sector are still limited. One important consideration amongst the limiting factors is the lack of standardisation and reliable metrics to evaluate the suggested methods [19]. SHM systems in practice are more commonly seen in offshore wind turbines as per the review of Martinez-Luengo et al [20].

### **1.3 Thesis Objectives and Overview**

In the previous subsection a brief overview of the research around SHM was presented. Craving the benefits of transitioning to a condition-based maintenance scheme, which empowers the vision of increased service performance and safety of operation in a sustainable future for the industry and driven from the ideas in the literature presented above, came inspiration for the present thesis.

More specifically, the purpose of this study is to explore the capabilities of different data driven models as the backbone of SHM system for indirect plate thinning detection on a fictitious structural domain under high operational variability. The idea was to investigate various parameters such as sensor topology, damage severity and their influence on different SPR approaches. The following paragraphs briefly introduce the reader in the procedure followed to achieve this purpose and the key thoughts behind each decision.

In this work, a fictitious, plate-like structural entity was selected. The choice of this simplified structural domain extricates the analysis from the need of developing an accurate model of a real-world complex structure. Moreover, possible complicated effects of geometrical nature are avoided, hence, a more clear, direct view of parameter influence on the problem is thought to be observed which hopefully would allow for qualitative deductions to be made that could be generalised for different applications.

An additional challenge in modeling naval structures is the stochastic nature of their operational profile. The marine environment is modeled in a probabilistic manner, thus, designing and studying models in determined loading scenarios may not be representative of the real world. While several works, including some mentioned earlier, study strain-based SHM paradigms, the effects of the inherent probabilistic nature of reality on detection ability are not formally taken into account. In the present study high operational variability was modeled in the input by introducing several parameters as random variables and is thought to be a novel feature of this work. The structural domain was considered to be subjected to distributed pressure loads of random peak magnitude and location.

Two types of damage were modelled. A global, uniform thickness reduction representing uniform corrosion and a localised, contained uniform thickness reduction at random locations representing pitting corrosion.

The data required for applying the SPR methods of interest were generated by repeatedly solving models of the problem with FEA, each time using different sampled values for the random parameters, constituting Monte Carlo Simulations (MCS). It could be said that damage is not meaningful without a comparison between two different states of the system [7]. Accordingly, in this work where SPR is of concern, there needed to be two discrete states of the system. Measurements for both the healthy state of the structure and damaged states were extracted from



MCS. Since the data were produced in a controlled, virtual, experimental environment, the measurements were indisputably labeled and were split to be used for training and evaluating the classifiers.

Different locations for strain measurements were taken into account to introduce the concept of alternative sensor arrangements. The goal was to study the effect of “sensor density” in the performance of the detectors. Four sensor arrangements were considered and strain measurements were extracted from the MCS at specified locations, simulating the different arrangements. At each sensor, two longitudinal components and the shear in-plane stress are measured.

Four supervised learning SPR methods were applied. The Discordant Outlier Method, the Likelihood Ratio Test, Quadratic Discriminant Analysis and an Artificial Neural Network were employed and assessed. Furthermore, Principal Component Analysis, a tool from unsupervised learning, was introduced to explore the impact of data preprocessing and/or dimensionality reduction in the performance of the classifiers. The detectors were evaluated based on two metrics; the probability of correctly identifying existence of damage (POD) and the rate of falsely detecting damage (FAR) in the system.

Summarising, this study aims at indirect plate thinning detection using a strain-based SHM application. A simplified plate structure under probabilistic loading was considered. Strain data were generated with MCS of a FE model taking into account different sensor arrangements. Different SPR frameworks were applied and assessed. A schematic overview of the work is presented in Figure 3 below.

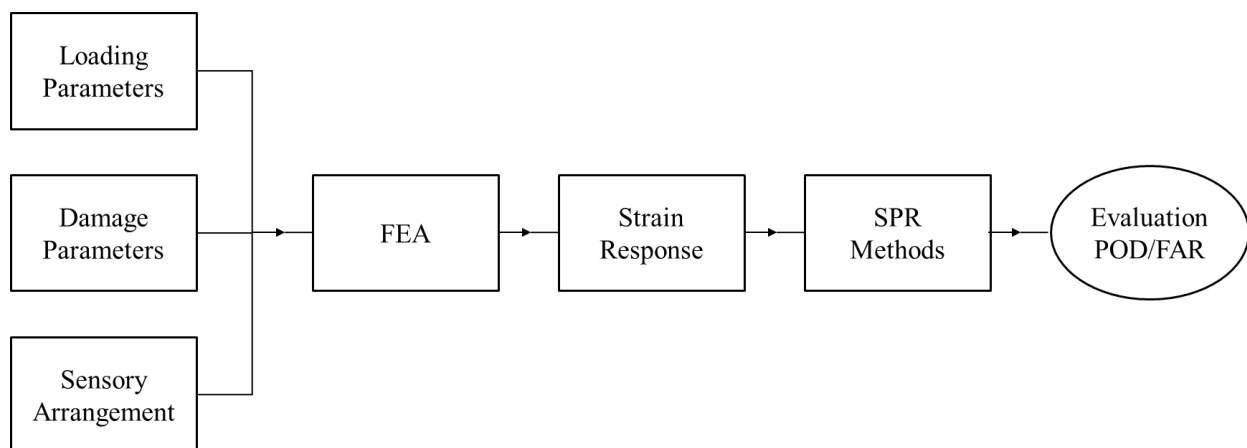


*Figure 3. Schematic overview of the present work.*

The following sections elaborate on the aforementioned topics and explain in depth the concepts applied and the steps taken towards accomplishing the objective of this thesis. Section 2 provides some theoretical insight regarding the framework around the concepts included in this study. Also, the foundation of the tools applied in this work as interpreted by the writer are briefly described. In Section 3 the development of the problem at hand and modelling details are explained. Section 4 describes the data construction and processing procedures followed by Section 5 in which the application of the detectors is presented along with a look into the results and relevant observations. Finally, Section 6 summarises this analysis, offers some final thoughts around the subject and provides inspiration for extensions in the future.

## 2 Theoretical Background

The introduction aimed to provide a first look into the ideas that inspired this work and a general overview of the procedures executed for the purposes of the present study. In this regard, the current section aims to introduce the reader to the theoretical foundations on which this work was based. For each topic, the basic concepts required to understand the succeeding chapters were included. The advanced reader can be directed to the literature referred along each subject for more specialised, holistic information.

The most important principles of SHM have already been introduced in Section 1.2. In those introductory paragraphs it was explained that in the present work, as in many of the aforementioned approaches in the literature, SHM is examined under the scope of SPR. Naturally, in the following subsections, elements from the field of SPR are described. Also, the mathematical framework of the SPR methods of interest is presented. Finally, the fundamentals of FEA are included.

### 2.1 Statistical Pattern Recognition (SPR)

The field of pattern recognition is concerned with the automated discovery of regularities in data. Pattern recognition and Machine Learning are basically different views of the same field with the first having its origins in engineering while the latter in computer science [21]. Statistical Pattern Recognition (SPR) is the subdomain of pattern recognition for which the use of statistics is employed to gain insight on data and then utilise the acquired information to infer generalised rules. In pattern recognition probability theory is used to acquire a consistent mathematical foundation for modeling uncertainty. This concept, coupled with decision theory, can provide a scheme for optimal decisions and accurate predictions. Applications of pattern recognition can involve classification and regression problems.

In this work, SPR is applied on a classification basis. To get a more formal view of SPR for classification purposes, given a number of discrete classes  $C_i$ , a classification algorithm is tasked with assigning an observation  $x_i$  to the corresponding class following a set of conditions  $K_i$ . The classification process takes the form of Eq. 2.1. Different algorithms make use of different mathematical approaches to generate alternative classification criteria.

$$\text{if } K_i \text{ is true then } x_i \in C_i \quad \text{Eq. 2.1}$$

The present work requires the detection of damage in a structural domain. Due to the fact that interest is focused in identifying the existence or absence of damage, this problem is tackled as a binary classification problem. Different SPR methods are employed to compare their performance on the specific problem. The theoretical background of those SPR methods utilised in the present work is described in the following subsections.

### 2.1.1 Likelihood Ratio Test (LRT)

The Likelihood Ratio Test (LRT) is a classical method in statistical hypothesis testing belonging to the Bayesian framework for pattern classification [22, 23]. Although the LRT method is most effective when the statistical nature of the subject classes is known, it is useful as a baseline to compare performance with the other detectors.

Let  $X_1, X_2, \dots, X_n$  be a set of random variables with a joint probability density function (PDF)  $f_{X_1 X_2 \dots X_n}(x_1, x_2, \dots, x_n; \theta)$ , where  $\theta$  is a statistical parameter. Then, consider the column vector  $\boldsymbol{\varepsilon}_i = [x_1^{\{i\}}, x_2^{\{i\}}, \dots, x_n^{\{i\}}]$  containing an observation for each random variable in the aforementioned set. Consider the following hypothesis scenario based on the parameter  $\theta$ :

$$\begin{cases} H_0: & \theta = \theta_0 \\ H_1: & \theta = \theta_1 \end{cases} \quad \text{Eq. 2.2}$$

In the LRT approach, observations are classified depending on the value of the ratio ( $\gamma_i$ ) between the likelihoods ( $L$ ), defined in Eq. 2.3, that each measurement vector ( $\boldsymbol{\varepsilon}_i$ ) belongs to a given class ( $H_i$ ) as seen in Eq. 2.4.

$$L(\theta) = f_{X_1 X_2 \dots X_n}(x_1, x_2, \dots, x_n; \theta) \quad \text{Eq. 2.3}$$

$$\gamma_i = \frac{L(\theta_0)}{L(\theta_1)} = \frac{f_{X_1 X_2 \dots X_n}(\boldsymbol{\varepsilon}_i; \theta_0)}{f_{X_1 X_2 \dots X_n}(\boldsymbol{\varepsilon}_i; \theta_1)} \quad \text{Eq. 2.4}$$

An alternative equivalent expression of the above would be the following:

$$\gamma_i(\boldsymbol{\varepsilon}_i) = \frac{p(H_0|\boldsymbol{\varepsilon}_i)}{p(H_1|\boldsymbol{\varepsilon}_i)} \quad \text{Eq. 2.5}$$

Combining Bayes rule (Eq. 2.6) with Eq. 2.5 above, and considering equiprobable prior probabilities for the two classes  $p(H) = p(D)$ , an assumption that will be justified for the problem at hand in section 5.1.1, the likelihood ratio can be calculated as the ratio of the class-conditioned PDFs of the measurements. Following the mathematical steps described above, the alternative expression of Eq. 2.7 occurs.

$$p(A|B) = \frac{p(B|A) p(A)}{p(B)} \quad \text{Eq. 2.6}$$

$$\gamma_i = \frac{p(\boldsymbol{\varepsilon}_i|H_0)}{p(\boldsymbol{\varepsilon}_i|H_1)} \quad \text{Eq. 2.7}$$

What remains to construct a classification algorithm based on the above ratio is a threshold ( $c$ ) controlling the decision boundary. Therefore, the following decision rule is derived:

$$\begin{cases} H_0: & \gamma_i > c \\ H_1: & \gamma_i < c \end{cases} \quad \text{Eq. 2.8}$$

It should be noted that the value of the classification threshold influences the confidence of the test and can be adjusted for calibrating the test according to the requirements of each application.

### 2.1.2 Discordant Outlier Analysis

Another method for classification employed in this study was discordant outlier analysis. For binary classification, in this approach, the decision regarding the measurement to be classified is determined by a metric which expresses distance between the measured vector and the center of the distribution of one of the classes, chosen as a basis. Suppose that class  $H_0$ , as per the notation followed in the previous subsection, is chosen as the basis.

In case the measured vector ( $\boldsymbol{\varepsilon}$ ) consists of a single measured variable, a univariate feature vector, the classification metric was decided to be the ‘z-score’ of a measurement, which is defined in Eq. 2.17 below.

$$z_i = \frac{\varepsilon_i - \mu_{H_0}}{\sigma_{H_0}} \quad \text{Eq. 2.9}$$

where  $\mu_{H_0}$  is the mean and  $\sigma_{H_0}$  the standard deviation of the base class.

The decision threshold must also be based on a univariate distribution with an inverse cumulative distribution function (CDF), symbolized  $\Phi^{-1}(\alpha)$ . The distribution is fitted on data from the base class. The constant  $\alpha$  is a design parameter that determines the level of desired confidence that measurement  $\varepsilon_i$  falls within the base class.

Taking into account the above considerations, the classification rule can be formulated as:

$$\begin{cases} \text{if } z_i < \Phi^{-1}(\alpha) \Rightarrow \text{Class } H_0 \\ \text{if } z_i > \Phi^{-1}(\alpha) \Rightarrow \text{Class } H_1 \end{cases} \quad \text{Eq. 2.10}$$

In case when the measured vector ( $\varepsilon$ ) contains multiple feature variables, a multivariate feature vector, the classification metric employed was the Mahalanobis distance, defined below as:

$$d_M^2 = (\varepsilon_i - \mu_{H_0})^T S^{-1} (\varepsilon_i - \mu_{H_0}) \quad \text{Eq. 2.11}$$

where  $S$  corresponds to the positive semi-definite covariance matrix for the  $H_0$  class distribution. Noting that the squared Mahalanobis distance is calculated, the decision threshold was derived from a chi-squared distribution fitted on base class data. The number of degrees of freedom ( $k$ ) of the distribution were equal to the length of the feature vector. In direct analogy with the case of the univariate vector, the value of the threshold was calculated by the inverse CDF of the chi-squared, symbolised as  $\Psi(a, k)$ . Therefore, the classification rule for a multivariate feature vector can be formulated as:

$$\begin{cases} \text{if } d_M^2 < \Psi(a, k) \Rightarrow \text{Class } H_0 \\ \text{if } d_M^2 > \Psi(a, k) \Rightarrow \text{Class } H_1 \end{cases} \quad \text{Eq. 2.12}$$

### 2.1.3 Quadratic Discriminant Analysis (QDA)

Quadratic Discriminant Analysis (QDA) refers to a classifier framework which has closed-form solutions that can be easily computed, are inherently multiclass, have proven to work well in practice and have no hyperparameters to tune [24]. As implied by the title, QDA forms a quadratic

hyperplane decision boundary. In this approach, an observation is assigned to the class that maximises the corresponding posterior probability  $P(C_i|\boldsymbol{\varepsilon}_i)$ , where  $C_i$  corresponds to a specific class and  $\boldsymbol{\varepsilon}_i$  to the available observation vector. The present detection method is modeled around the normal distribution. Hence,  $P$  is modeled as a multivariate normal distribution with density:

$$P(\boldsymbol{\varepsilon}_i|C_i) = \frac{1}{\sqrt{(2\pi)^d |\boldsymbol{\Sigma}_{C_i}|}} \exp\left(-\frac{1}{2}(\boldsymbol{\varepsilon}_i - \boldsymbol{\mu}_{C_i})^T \boldsymbol{\Sigma}_{C_i}^{-1}(\boldsymbol{\varepsilon}_i - \boldsymbol{\mu}_{C_i})\right) \quad \text{Eq. 2.13}$$

where  $d$  is the number of features in  $\boldsymbol{\varepsilon}_i$ , while  $\boldsymbol{\mu}_{C_i}$  is the mean vector and  $\boldsymbol{\Sigma}_{C_i}$  the covariance matrix of class  $C_i$ .

Assuming equal covariance matrices between the classes, the method is reduced to what is known as Linear Discriminant Analysis (LDA), which, as expected, is related to a linear discrimination boundary. LDA offers reduced computational requirements and in applications where the assumption of equal covariances is true or is a reasonable approximation of reality, then the performance remains the same with reduced computational cost. Figure 4 below offers a visual representation of the property described above. More specifically, LDA and QDA decision boundaries between two classes are drawn for two-dimensional data on a plane. The two variants of the method are compared between a case where the two classes have no significant difference in covariance and a case with different covariance patterns.

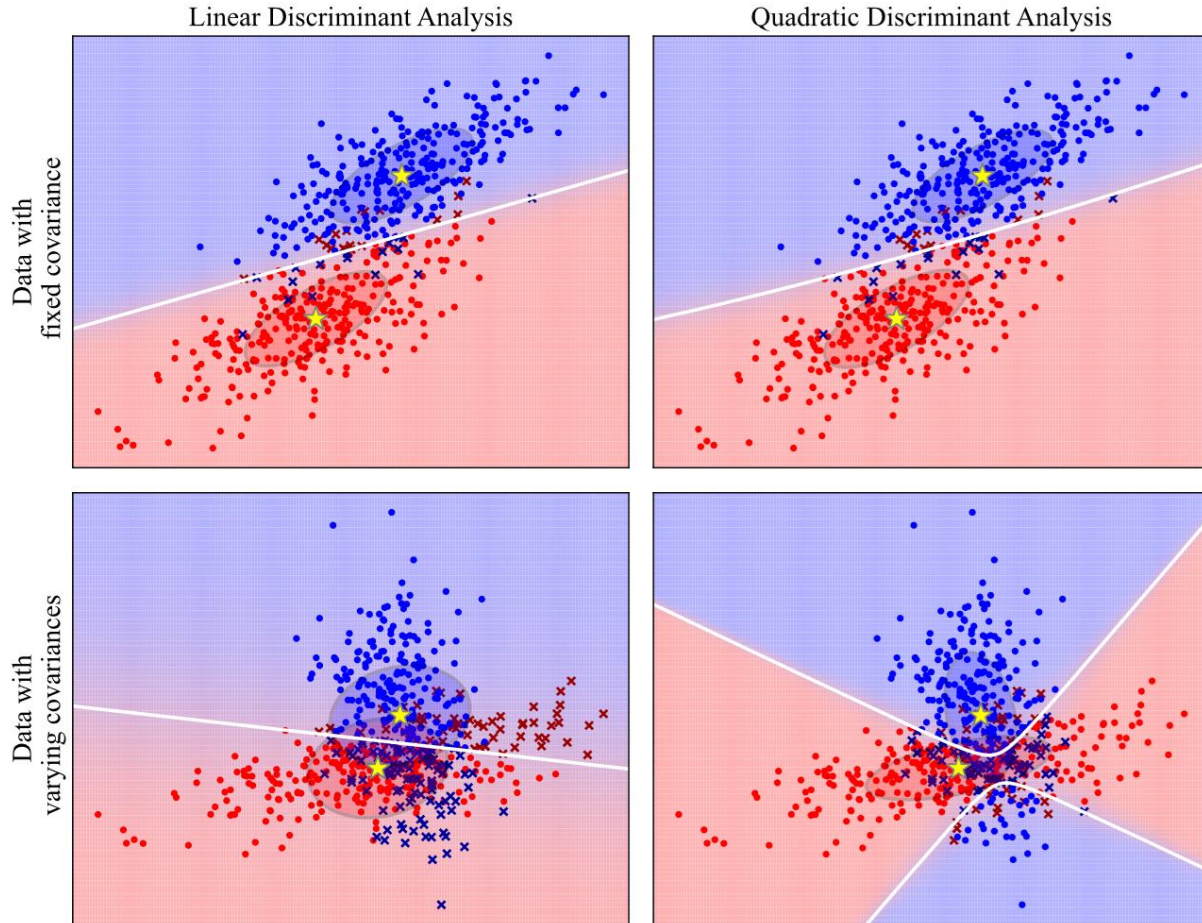


Figure 4. Decision boundary visualisation for QDA and LDA on different generic datasets. Comparison between the two variants in different data scenarios. (Source: Scikit-learn [25] (edited)).

Regarding the mathematical formulation of this method, using bayes rule (Eq. 2.6) and the law of total probability to express the posterior probability, Eq. 2.14 occurs.

$$P(C_i|\boldsymbol{\varepsilon}_i) = \frac{P(\boldsymbol{\varepsilon}_i|C_i) \cdot P(C_i)}{P(\boldsymbol{\varepsilon}_i)} = \frac{P(\boldsymbol{\varepsilon}_i|C_i) \cdot P(C_i)}{\sum_j P(\boldsymbol{\varepsilon}_i|C_j) \cdot P(C_j)} \quad \text{Eq. 2.14}$$

LDA and QDA revolve around maximising the aforementioned posterior. The latter is equivalent to maximising the natural logarithm of the posterior. Considering that this is not the primary interest of this work, the mathematical processing will be omitted. The interested reader can find the subsequent math in works such as those of Farrar [7] and Murphy [26]. Briefly mentioned, by applying the natural logarithm on both parts of Eq. 2.14, substituting the density of the normal distribution where possible, seeking the maximum posterior produces the following:



$$\begin{aligned} & \boldsymbol{\varepsilon}_i^T (\mathbf{S}_H - \mathbf{S}_D)^{-1} \boldsymbol{\varepsilon}_i + 2(\mathbf{S}_D^{-1} \boldsymbol{\mu}_D - \mathbf{S}_H^{-1} \boldsymbol{\mu}_H)^T \boldsymbol{\varepsilon}_i + (\boldsymbol{\mu}_H^T \mathbf{S}_H^{-1} \boldsymbol{\mu}_H - \boldsymbol{\mu}_D^T \mathbf{S}_D^{-1} \boldsymbol{\mu}_D) \\ & + \ln \left( \frac{|\mathbf{S}_H|}{|\mathbf{S}_D|} \right) + 2 \ln \left( \frac{p_D}{p_H} \right) = 0 \end{aligned} \quad \text{Eq. 2.15}$$

It should be mentioned that in the formulation of Eq. 2.15 above it was assumed that QDA is applied on a binary classification problem between two classes noted with the subscripts “ $H$ ” and “ $D$ ”, in tandem with the problem addressed in this study. The terms  $p_H$  and  $p_D$  represent the prior probabilities for the two classes. Regarding the rest of the terms  $\boldsymbol{\mu}_j$  is the mean vector and  $\mathbf{S}_j$  the covariance matrix of class  $C_j$ .

Notably, Eq. 2.15 is quadratic with respect to  $\boldsymbol{\varepsilon}$ , hence, the resulting decision boundary is too. Setting the left-hand side of the equation equal to  $\delta_Q(\boldsymbol{\varepsilon}_i)$ , the classification algorithm can be summarized by the following decision rule:

$$\begin{cases} \text{if } \delta_Q(\boldsymbol{\varepsilon}_i) < 0 \Rightarrow \boldsymbol{\varepsilon}_i \in H \\ \text{if } \delta_Q(\boldsymbol{\varepsilon}_i) > 0 \Rightarrow \boldsymbol{\varepsilon}_i \in D \end{cases} \quad \text{Eq. 2.16}$$

## 2.2 Principal Components Analysis

Principal Component Analysis (PCA) is a process used to change the basis of input data into a new basis formed of principal components (PCs). The PCs constitute an orthonormal basis of linearly uncorrelated data dimensions. Each principal component successively holds the maximum variance for the data [27]. The latter property of the PCs is exploited in data analysis to perform dimensionality reduction. It is assumed that axes with the most variance hold the most information. As a result, it is common to reduce dimensionality of a problem by applying PCA on the data and then keeping that number of PCs that accounts for a desired amount of retained variance.

Essentially, PCA is computationally equivalent to applying Singular Value Decomposition (SVD) on data that have been pre-processed by mean subtraction and reshaped to unit variance. In principle, SVD is a data-driven method that can produce a hierarchical basis in terms of dominant patterns to represent high-dimensional correlated data. A big advantage of this is that these patterns are discovered solely based on the data without human expertise required. Furthermore, cluster formation is inherent to the PCA process. This clustering is very useful for pattern recognition and

classification purposes [28]. In this regard, it was decided to analyse the impact of PCA of the input data in the classification processes applied in this study.

Figure 5 aims to visually enhance the understanding of principal components as the linearly uncorrelated (orthogonal) directions of maximum variation in a simplified paradigm. Two vectors representing the direction of the two principal components are plotted on a scatterplot of bivariate gaussian data.

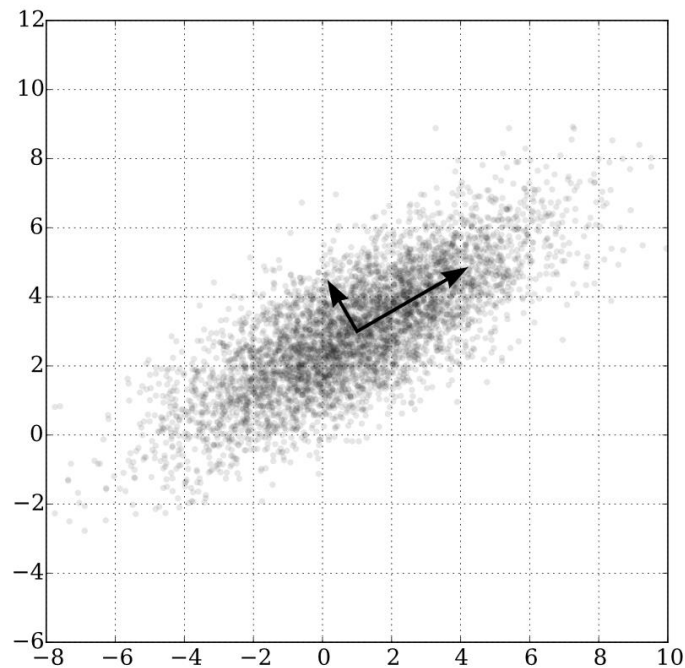


*Figure 5. Visual representation of the direction of two PCs on bivariate gaussian data. (Source: Wikipedia [29])*

## 2.3 Artificial Neural Networks (ANNs)

### 2.3.1 Introduction to Artificial Intelligence, Machine Learning and ANNs

In the recent years, processes of the field of Artificial Intelligence (AI), especially from the subdomain of Machine Learning (ML), have been increasingly adopted in an ever-broadening number of scientific and business sectors. Essentially, ML methods are data-driven processes that are able to extract useful information from input data and can be utilised to gain deeper insight on new data, or make predictions. The resulting information can drastically improve decision making. In today's digitalised world, where information is abundant, the control and understanding of it

provides unprecedented advantages. It is only natural that interest in the research and implementation of ML has risen tremendously.

There are three types of Machine Learning: supervised learning, unsupervised learning, and reinforcement learning. Supervised learning requires the availability of “labeled” training data, a series of inputs with known outputs to be used to train a model. Then, the trained model can be used to process data of interest and predict the outputs. In unsupervised learning, ML models are used to extract useful representations or information about the underlying structure of data of interest. Finally, in reinforcement learning the goal is developing models that improve their performance based on a reward signal from interactions with their environment and is a trial-and-error approach [30]. The present study focuses on supervised learning, as the problem at hand is a binary classification one, aiming at discriminating between existence of damage or not, based on fully labeled data derived from FEA.

Deep Learning is a subfield of ML in which information is processed successively in multistage operations. The term “deep” should not be misinterpreted as relating to some form of higher understanding. Rather, it refers to the multilayer structure of such models. Artificial Neural Networks (ANNs) were inspired by the biology of the brain, yet they should not be confused as models of the brain. ANNs is a term used interchangeably with deep-learning, as ANN models are the dominant mathematical framework for deep learning. Although there are different, complex architectures of neural networks, this study focuses on the feedforward, back-propagation ANN type.

ANNs consist of an interconnected series of layers, each made up of a number of neurons or nodes. Every neuron processes a part of information. An input signal from one or more previous neurons is received by each neuron. An operation is applied to the input signal according to the instructions of individual neuron that are stored in it as a weight ( $w_i$ ) value. The processed signal is then transmitted to one or more succeeding neurons. The first layer of an ANN is responsible for handling the input data. The final layer is responsible for the output, which depends on the application and may be probability values in case of classification problems or could also be continuous values in case of regression problems [31]. A typical architecture of a multilayered ANN is schematically presented in Figure 6. A brief description about each of the individual components that constitute the aforementioned architecture is given in the following paragraphs.

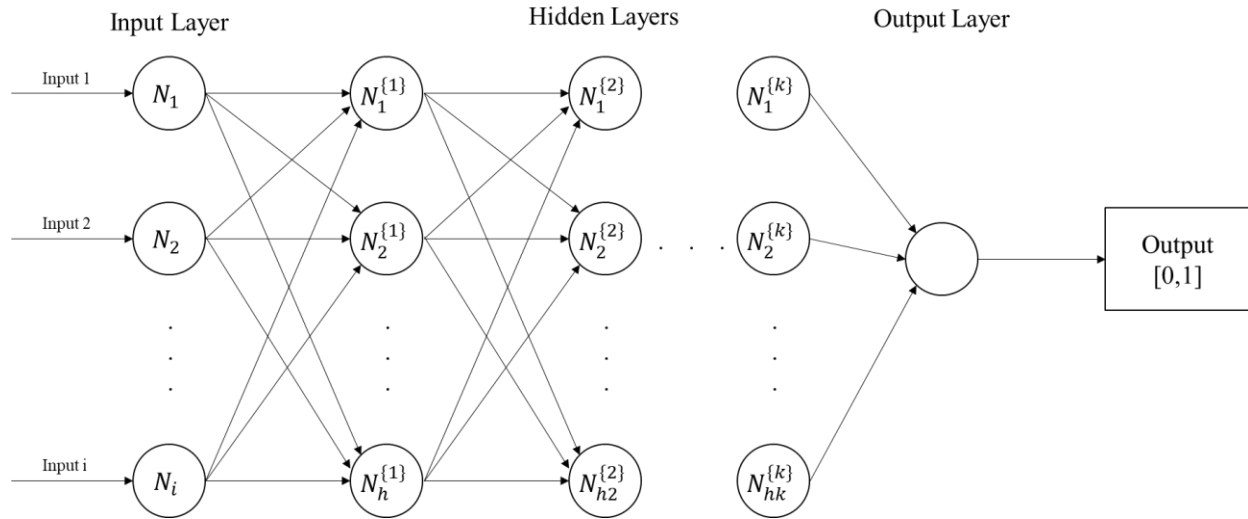


Figure 6. Schematic representation of multilayered feed-forward ANN for binary classification.

### 2.3.2 Artificial Neuron Modeling

The neuron is the fundamental information-processing operator of an ANN. Figure 7 depicts a schematic representation of a typical neuron. Firstly, the input signals  $x_i$  and bias are summed using the corresponding weights according to Eq. 2.17. The output of the summing junction is then input in an activation function, as per Eq. 2.18, forming the signal appropriately as input for the next layer of neurons or even as the final output of the network. The weight values constitute the “knowledge” of the network and are adjusted during the training process. The bias is a fixed term used for parametrising the activation function, allowing to shift it to best fit the data.

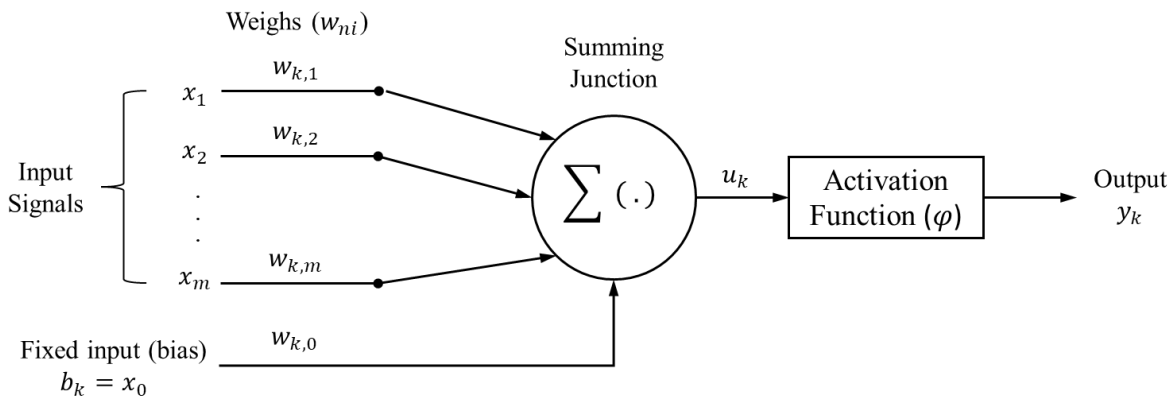


Figure 7. Schematic representation of an artificial neuron.

$$u_k = \sum_{i=1}^m w_{k,i}x_i + b_k = \sum_{i=0}^m w_{k,i}x_i \quad \text{Eq. 2.17}$$

$$y_k = \varphi(u_k) \quad \text{Eq. 2.18}$$

The above model of artificial neuron constitutes a linear binary classifier by itself, commonly referred to as the Perceptron or Rosenblatt neuron [32], but despite its innovative design back in the day, its applications are limited. A multilayered ANN consists of an input, an output and at least a hidden layer between them. The presence of a non-linear activation function is crucial in the architecture of multilayered ANNs. The summation process is a linear operation, consequently, the output of stacking multiple layers would still be equivalent to another linear transformation. Hence the application of a non-linear activation function is fundamental in deploying multilayer networks that effectively process input signals.

### 2.3.3 Activation Functions

Apart from introducing non-linearity in the model, the activation function is important in the performance of the ANN as well as forming the output signal appropriately for the application at hand. The activation function controls the output of a neuron according to the input signals. Functions with different characteristics offer different learning properties. The steepness, range and differentiability of the function can affect the learning rate. Some of the most commonly used types of functions are briefly presented in the paragraphs that follow.

One of the simplest activation functions used is the binary step function. The step function acts like a threshold that determines the “firing” or not of the neuron. The mathematical formulation of the unit step function is seen in Eq. 2.1 while an indicative graph of the unit step function is shown in Figure 8.

$$\varphi(u) = \begin{cases} 1 & \text{if } u \geq 0 \\ 0 & \text{if } u < 0 \end{cases} \quad \text{Eq. 2.1}$$

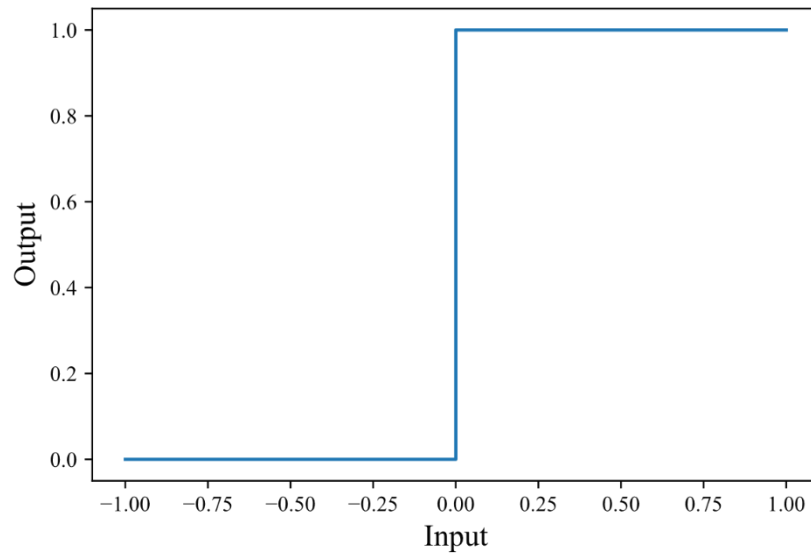


Figure 8. Indicative unit step function plot.

Another popular activation function is the hyperbolic tangent function. The later projects the input signal in the  $[-1,1]$  interval. This function is popular with binary classification problems. The mathematical formulation of the hyperbolic tangent function is seen in Eq. 2.19 while an indicative graph is shown in Figure 9.

$$\varphi(u) = \frac{e^{2u} - 1}{e^{2u} + 1} \quad \text{Eq. 2.19}$$

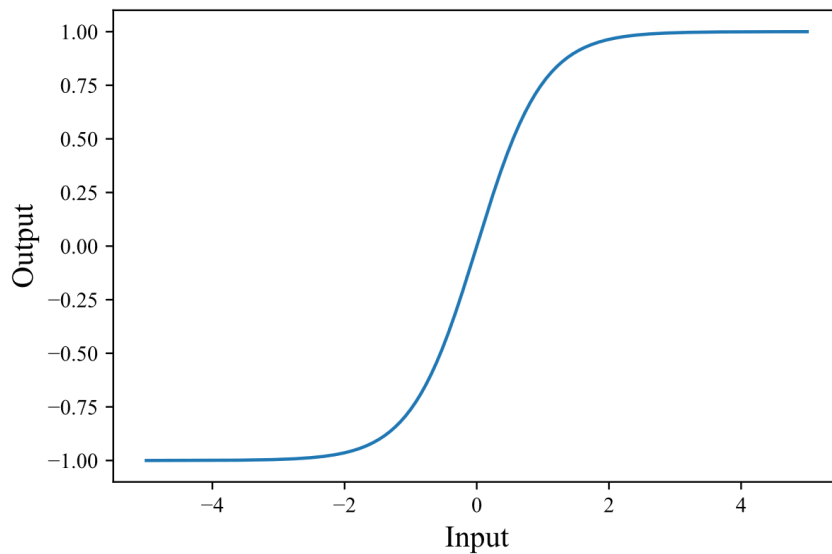
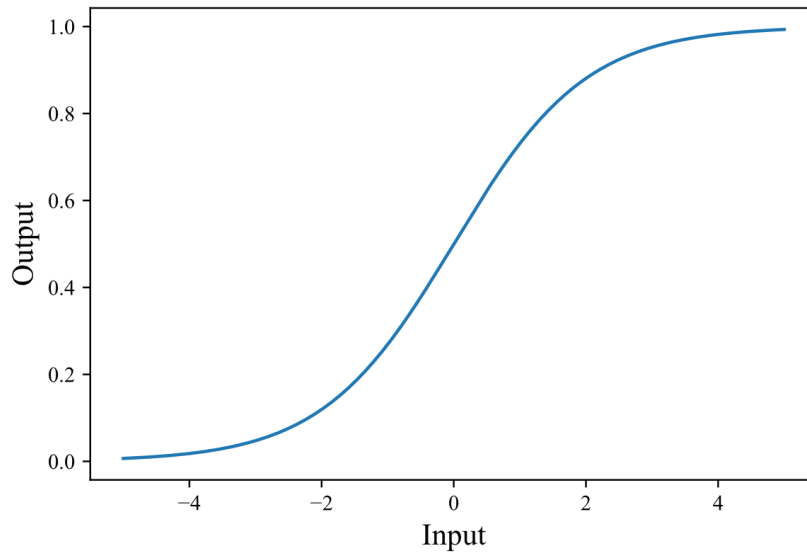


Figure 9. Indicative hyperbolic tangent function plot.

Similar to the hyperbolic tangent, the sigmoid function is an s-shaped curve which transcends the input in the  $[0,1]$  range. Therefore, it is particularly useful when the desired output is probabilities. The mathematical formulation of the sigmoid function is seen in Eq. 2.20 while an indicative graph is shown in Figure 10.

$$\varphi(u) = \frac{e^u}{e^u + 1} \quad \text{Eq. 2.20}$$



*Figure 10. Indicative sigmoid function plot.*

Finally, perhaps the most popular activation function in ANNs is the rectified linear unit function (ReLU), it is widely used in convolutional networks. One useful property of the present function is that it does not require all the neurons to “fire” at once. The mathematical formulation of the ReLU function is seen in Eq. 2.21 while an indicative graph is shown in Figure 11.

$$\varphi(u) = \max(0, u) \quad \text{Eq. 2.21}$$

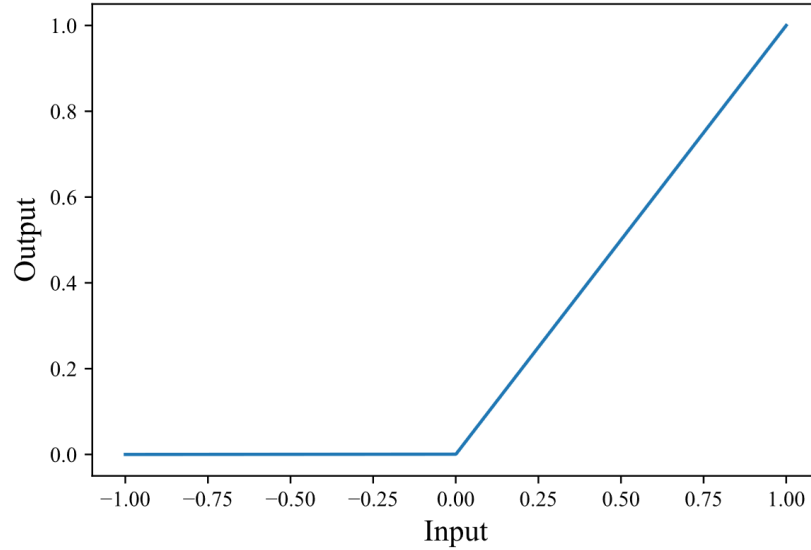


Figure 11. Indicative ReLU function plot.

### 2.3.4 ANN Training Process

An ANN model is trained by iterating over training data. The process of “learning” involves passing the data through the system. Then the predicted outcome is evaluated based on the desired outcome using a loss function  $J$ . The loss function offers a metric that determines how the model is adjusted during training in order to minimise the loss. For models designed for regression problems, popular loss functions are the Mean Square Error (Eq. 2.22) and Mean Absolute Error (Eq. 2.23). For classification problems, the Binary (Eq. 2.24) and Categorical (Eq. 2.25) Cross-Entropy functions are deployed.

Let  $\hat{y}$  denote the predicted variable and  $y$  the target variables,  $m$  is the number of training samples,  $c$  is the number of classes in a classification problem. Then, the aforementioned loss functions can be formulated as:

$$J = \frac{1}{m} \sum_{i=1}^m (y_i - \hat{y}_i)^2 \quad \text{Eq. 2.22}$$

$$J = \frac{1}{m} \sum_{i=1}^m |y_i - \hat{y}_i| \quad \text{Eq. 2.23}$$



$$J = -\frac{1}{m} \sum_{i=1}^m y_i \log(\hat{y}_i) + (1 - y_i) \log(1 - \hat{y}_i) \quad \text{Eq. 2.24}$$

$$J = -\frac{1}{m} \sum_{i=1}^m \sum_{j=1}^c y_{ij} \log(\hat{y}_{ij}) \quad \text{Eq. 2.25}$$

“Knowledge” is stored in the weights of the neurons. The model is initialised with random weights and is continuously adjusted during training. The process of adjusting the model is complicated and is crucial in the successful shaping of the model. A suboptimal selection of parameters for the training can lead to inaccurate models or it can cause overfitting. Overfitting is, in essence, developing a model that specifically mapped the training data and is unable to generalise, as a result achieving inferior performance on new data.

One of the most popular algorithms for adjusting the weights of an ANN is the Stochastic Gradient Descent (SGD). Briefly, in SGD randomly drawn batches are input to the model and then the loss function is calculated for each set of predicted and target variables. The gradient of the loss function ( $\nabla J$ ) with respect to the vector of the model parameters ( $\theta$ ), the vector of all the weights and biases, is calculated for each batch. The weights are shifted to the opposite direction of the gradient, reducing the loss on the batch by a little. This process propagates the error backwards through the network and is related to the term back-propagation describing the specific architecture. The step of the shift is controlled by the learning rate parameter ( $\alpha$ ). The value of the learning rate is crucial for successfully training the model. By adjusting this rate appropriately, the training loop can effectively avoid local minima and descend to the true minimum, while the required training time is also heavily dependent on this value. The mathematical description of SGD is presented in Eq. 2.28. In Figure 12 a visual representation of the SGD process on an indicative three-dimensional loss surface is presented.

$$\theta = [w_1, w_2, \dots, w_n]^T \quad \text{Eq. 2.26}$$

$$\nabla J(\theta) = \left[ \frac{\partial J}{\partial w_1}, \frac{\partial J}{\partial w_2}, \dots, \frac{\partial J}{\partial w_n} \right] \quad \text{Eq. 2.27}$$

$$\theta := \theta - \alpha \nabla J(\theta) \quad \text{Eq. 2.28}$$

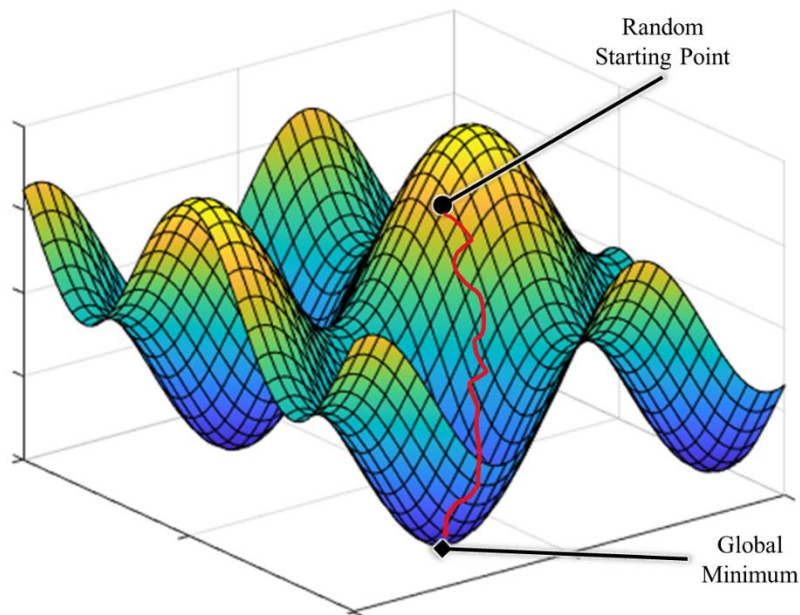


*Figure 12. Visualisation of an indicative successful loss minimisation path on a loss surface via SGD.  
(Source: [33](edited))*

After the training process is complete, the model is ready to be used to make predictions on new data of interest.

### 2.3.5 Summary

One advantage of the use of ANNs is their ability to manually extract features from the data [31]. The tedious task of feature engineering that requires great expertise can be automated with the use of ANNs. Each layer of an ANN can be thought of as a filter that extracts representations of the data that could potentially be more meaningful for the application of interest. The number of nodes in a layer represents the dimensionality of the space in which data is represented in the current layer. Increasing the number of nodes allows for seeking higher dimension decision boundaries, possibly leading to a more accurate classification model. Depending on the nature of each problem, increasing the dimensionality could lead to discovery of unwanted patterns, hence overfitting the model.

A very intuitive description of the ability of ANNs to explore decision boundaries is to think of data classes as sheets of different-coloured paper [31]. Imagine the sheets stacked on top of one another and then crumpled, the result is a single paper ball in which the boundaries between

different-coloured sheets are unclear. This paper ball can be viewed as an analogy to the input data intended to be analysed by the ANN. Each layer of the ANN essentially acts as a transformation of the data in space. In deep learning, the complex geometrical transformation required to separate the different classes is broken down into a long series of rudimentary ones. The final result of an effective network would be clearly separated sheets of coloured paper.

## **2.4 Fundamentals of Finite Element Analysis (FEA)**

The mathematical methodologies described in the previous subsections are data driven. Subsequently, there occurs the need for relative data. The present investigation concerns a structural analysis problem. In order to acquire structural response data from a system of interest there are three potential approaches:

- a) Measurements from physical experiments at full or model scale.
- b) Analytical solutions of a mathematical physics model.
- c) Numerical approximations of a physics model.

The first approach is very limiting in terms of high costs of implementation, difficulty in controlling and replicating the required conditions, noisy measurements, sensor limitations and, of course, requires considerable amount of time to execute enough experiments. On the other hand, even in the presence of an accurate physical model, the necessary mathematical procedure to acquire the desired solutions may be intractable, depending on the complexity of the application of interest. The last approach, numerical approximations, overcomes the most of the preceding disadvantages. This approach, when implemented correctly, offers reasonable accuracy in the solution, can be precisely controlled and is scalable both in terms of number of experiments and magnitude of the application. The dominant framework for numerical approximations of physics based structural problems is Finite Element Analysis (FEA). It was deemed appropriate to include some basic theoretical elements of FEA to accompany the present study.

### **2.4.1 Basic Principles of the Finite Element Method**

The Finite Element Method (FEM) is essentially a simulation of the continuum as a series of fundamental elements interconnected at a finite number of points referred to as nodes. As far as

frames are concerned, which consist of a number of beams connected to each other at specific points, FE modeling is very intuitive since physical boundaries and connection points between members already exists (visual example presented in Figure 13). Regarding continuous structures such as the hull of a ship, or other plate like structures, where no physical discretisation is existent, the entire domain needs to be virtually separated into smaller constituting elements (visual example presented in Figure 14). The elements can be one-dimensional (beams), two-dimensional (triangular or rectangular) or even three-dimensional (tetrahedrals etc). The nodes are usually positioned on their corners or edges but can even be in the inside of the elements depending on the architecture of the element.

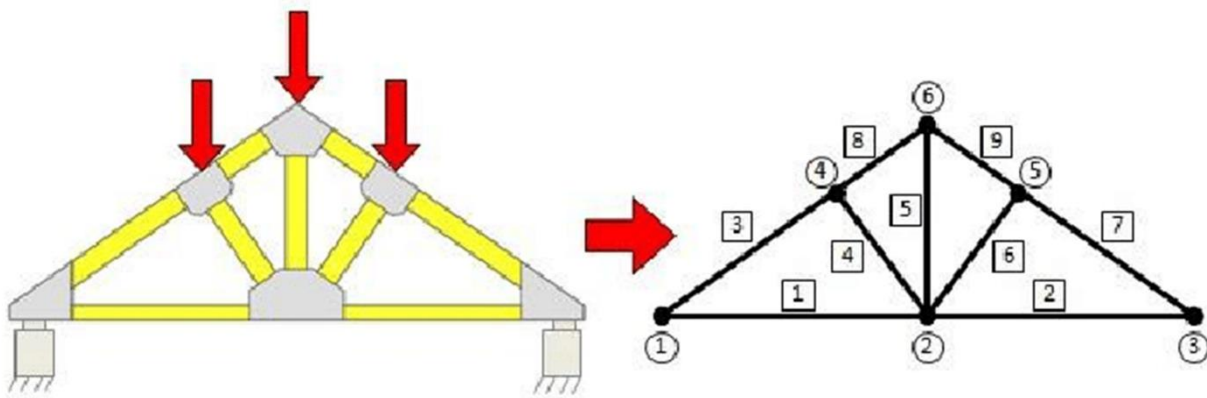


Figure 13. Example of discretisation of a 2D structural frame into a FE model consisting of nine elements and 6 nodes. (Source: [34])

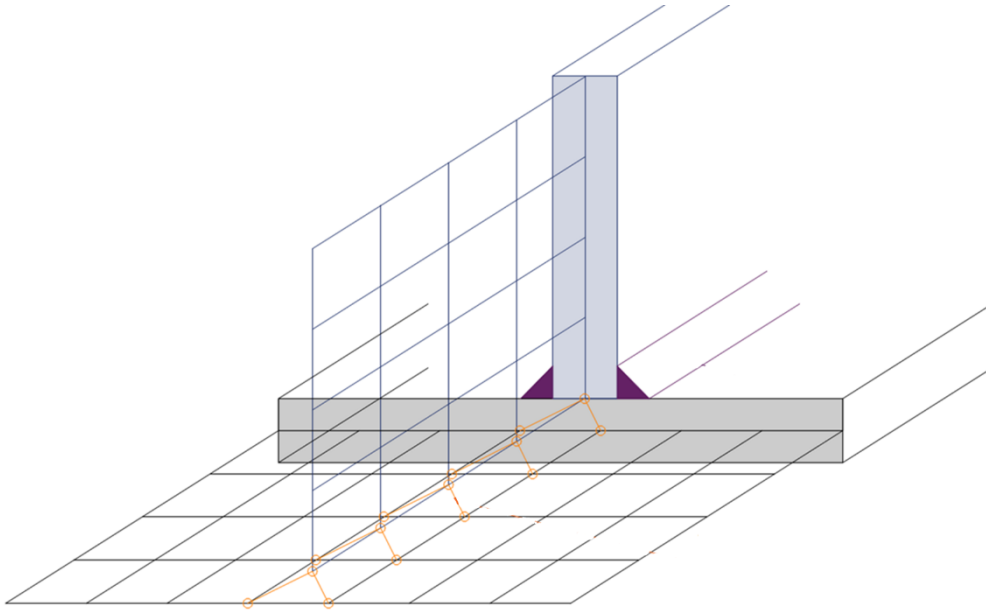


Figure 14. Example of FE modelling of a T joint between two thin-walled plates. (Source: [35])

The continuous domain is simulated as a series of discrete variables or degrees of freedom, usually defined as the nodal displacements and optionally their derivatives as well. Displacements inside each element must be compatible with the nodal displacements and are directly dependent on the corresponding values at the nodes. As a result, the structural response is approximated by calculating all nodal displacements. The continuous problem is therefore transformed into a discrete one. Acquiring the structural response comes down to forming the equilibrium equations at the nodes and then solving the resulting system with respect to nodal displacements.

To achieve an accurate solution, there are some conditions that need to be satisfied. Namely, conditions of equilibrium as well as geometrical continuity inside the elements and along their edges. It is interesting to note that a collection of elements connected only at their nodes is not a direct analogous of the continuum, as displacement continuity is only explicitly imposed at the nodes, thus gaps or overlaps between members can occur following this modelling approach (visual example presented in Figure 15). Of course, it should always be taken into consideration that the FEM is meant to approximate reality and is not expected to produce exact results.

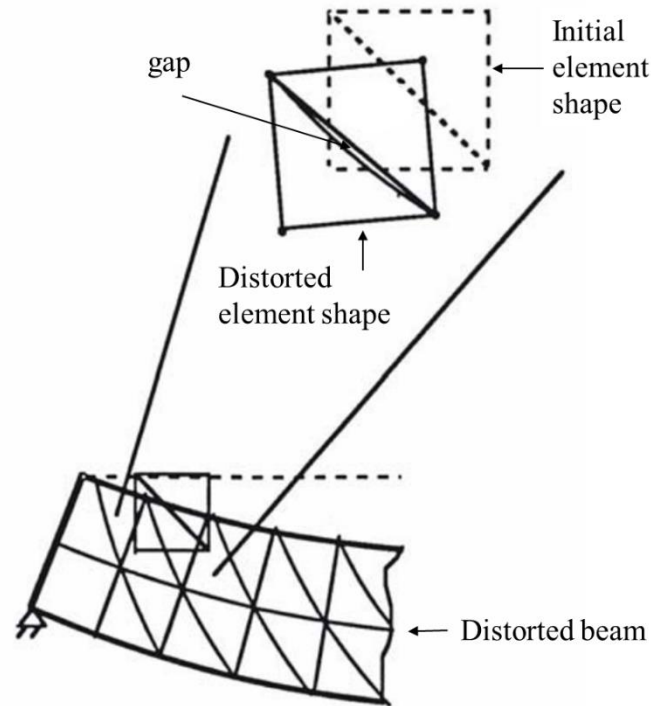


Figure 15. Example of gap forming between the edges of triangular elements in the distorted state. Case of modeling a beam cantilever with triangular shell elements. (Source: [36])

However, with the implementation of several technics, this inherent error can be mitigated to an acceptable level for each application. The simplest approach to reduce inaccuracies in FE modelling is by using an increased number of smaller elements. Increased accuracy by increasing the fidelity of the model comes at the cost of increased need of computational power and time requirements.

Nonetheless, there are more sophisticated methods to increase accuracy. More specifically, each element is characterised by its shape function. The shape function takes the nodal values of a field quantity (such as the displacement) and projects it throughout the entire elemental domain. Appropriate design of the shape function can guarantee equilibrium and geometrical continuity inside the elements and along their boundaries while only enforced at the nodes. Several element types and shape functions are available in the literature and are included in commercial FEA software, each optimised for a specific type of application. It is clear that careful selection of the element architecture is important in achieving greater solution accuracy.

In FEM, equilibrium is not necessarily satisfied at every location of the continuous domain. Regardless, there are two conditions that must always be satisfied. In particular these are:

- a) Equilibrium of forces (external and internal) on every node.
- b) Equilibrium of nodal forces of every element.

The aforementioned conditions are visually summarised in Figure 16.

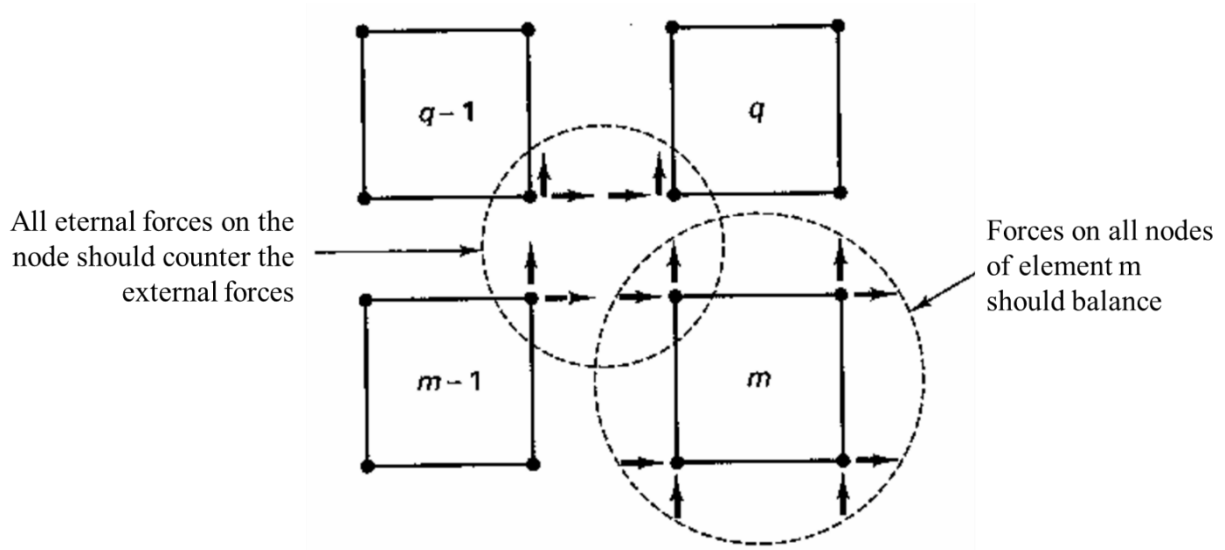


Figure 16. Visual explanation of elemental equilibrium and nodal equilibrium on an indicative FE mesh. (Source: [36])

The generalised form of the system of equilibrium equations of a FE model can be summarised in:

$$\{F\} = \{K\} \times \{U\} \quad \text{Eq. 2.29}$$

where  $\{F\}$  is the vector that contains all external force effects expressed as equivalent forces on every node.  $\{K\}$  is the global stiffness matrix of the system and  $\{U\}$  is the column vector containing all nodal displacements, the dependent variables or degrees of freedom (DOFs) of the system.

The global stiffness matrix ( $\{K\}$ ) is derived as a direct superposition of the stiffness matrix of every element ( $\{K\}^{(m)}$ ).

$$\{K\} = \sum_m \{K\}^{(m)} \quad \text{Eq. 2.30}$$

Commonly, the stiffness matrix of an element will be available in the literature regarding a specific element type. In general, the elemental stiffness matrix is expressed in terms of a local, on-element coordinate system. Before superimposing, each member stiffness matrix is expressed in terms of the selected global coordinates system and projected to the dimensions of the global stiffness matrix. Namely, a transformation to the coordinate system that is defined for the entire composite model is required. This global reference system does not coincide with the local systems of every element for most complex structures. The required transformation is executed with the use of a transformation matrix  $\{T\}$ , which incorporates all necessary rotational conversions to reposition the reference system of the initial matrix. This is described in mathematical terms in Eq. 2.31.

$$\{K\}^{(m)} = \{T\}^T \{\hat{K}\} \{T\} \quad \text{Eq. 2.31}$$

The  $\hat{\quad}$  notation is introduced to distinguish the matrixes which refer to the local coordinate system from their counterparts, those referring to the global coordinate system of the model.

Once the elemental stiffness matrices ( $\{K\}^{(m)}$ ) have been formulated and expressed in the global coordinate system, the stiffness matrix of the entire model can be constructed as shown in Eq. 2.30.

The subsequent step in establishing a FE model is to appropriately define any external loading and boundary conditions. The first are incorporated in  $\{F\}$  matrix, as introduced earlier. In the discretised reality of FEA, where all external forces should be applied on nodes, it is important that any concentrated point loads coincide with a node in the model. Consequently, operational conditions should be taken into account when discretising the model. It is made obvious that any distributed pressure loads are required to be discretised to equivalent point loads on node locations.

As far as boundary conditions are concerned, these can be integrated as constraints of DOF in the displacement vector  $\{U\}$ . Superficially, this procedure might be regarded as easy as setting some variable to a fixed value because of the way supports are modelled in classical mechanics theory. Nonetheless, when accuracy is desired, the application of idealised theoretical boundary conditions may not be acceptable. As a result, detailed modelling of the supports and boundary interactions may be required. For this matter, the analyst is expected to have ample theoretical knowledge and intuition regarding the problem at hand.



It is important to keep in mind that in modern FEA environments most of the heavy mathematical workload has been automated and assigned to computers. Nevertheless, appropriate modelling of the problem, as well as evaluation and interpretation of the results still require human expertise and should not be adopted without judgement. Often, results from FEA are compared directly to results acquired from analytical solutions or experimental measurements where applicable. This practice ensures validity of the modelling and in case of significant deviations indicates the need for potential adjustments.

#### **2.4.2 FE Modeling of Thin-walled Structures**

The general procedure of structural analysis using the FEM has been introduced in the previous subsection. In the present work, a thin-walled plate structure falls in the scope of analysis. It was considered appropriate to discuss some more details regarding modelling thin-walled structures in FEA.

Thin-walled structures are defined as these structures in which thickness is of much smaller magnitude than the rest of the dimensions. The prevalence of thin-walled components and structures in every domain is justified by their optimised nature in terms of material and weight economy. With clever geometrical modifications (e.g. stiffeners, corrugation) the desired stiffness and stability are achieved with significantly reduced thickness, resulting in less structure weight and less material requirements. Such thin-walled arrangements are common in marine constructions and include plates, bulkheads, stiffened panels, or even the entire hull, often regarded as a thin-walled hollow girder to study its response in global bending and twisting.

Thin-walled structures can be modeled using rectangular, flat, shell-type elements. Shell geometries are fully defined by their mid-surface and thickness. In general, a thin-walled arrangement will be subjected to bending as well as in plane stresses. Assuming operation in the range of small deformations, the deformations due to bending and due to the plane stress conditions can be considered independent [37]. In this regard, the shell element can be derived by superimposing a plane stress element with a bending element [36] as seen in Figure 17.

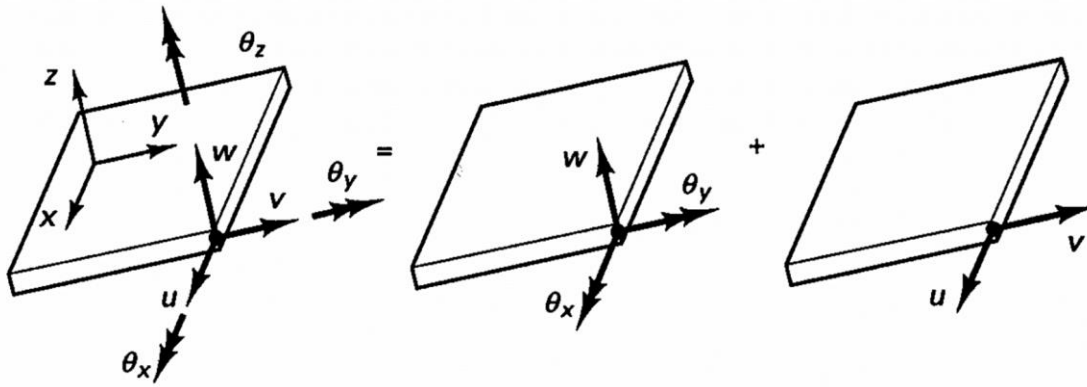


Figure 17. Modeling of a flat "shell" element by superimposing a "bending" and a "plane stress" element. (Source [36]).

This principle allows to simplify the formulation of the shell element, as its stiffness matrix can be produced by appropriately adding the stiffness matrices of the its other two components. The stiffness matrices  $\{\widehat{K}_B\}$  and  $\{\widehat{K}_P\}$  of the bending and plane stress elements accordingly are available in the literature [36].

The resulting stiffness matrix for the shell element can be produced as follows:

$$\{\widehat{K}_S\} = \begin{bmatrix} \{\widehat{K}_B\} & \{0\} \\ \{0\} & \{\widehat{K}_P\} \end{bmatrix} \quad \text{Eq. 2.32}$$

Since the bending model has three DOFs per node and a total of 4 nodes, the accompanying stiffness matrix will be 12x12 sized. Equivalently, for the plane stress element with two DOFs per node, the stiffness matrix will be 8x8 sized. Consequently, the stiffness matrix of the resulting shell element, as per the formulation of Eq. 2.32, will be a 20x20 matrix. In the aforementioned equation  $\{0\}$  symbolises appropriately shaped zero matrices.

In order to integrate the local, elemental stiffness matrix  $\{\widehat{K}_S\}$  of a shell element to the global stiffness matrix of an entire model, as mentioned in a previous paragraph, a transformation to the global coordinate system is required. Similarly, the transformation can be written as follows.

$$\{K\}^{(m)} = \{T\}^T \{\widehat{K}_S\} \{T\} \quad \text{Eq. 2.33}$$

Consequently, to model a thin-walled structure the discretisation of its geometry must be decided, taking into account the loading conditions and any relevant constraints. The global stiffness matrix describing the entire model can then be constructed as per Eq. 2.30.

Following the methodology of the previous subsection, the loads should be discretised and incorporated in the forces vector. Then the boundary conditions should be modelled appropriately and expressed in terms of constraints of DOF in the displacement vector. Once the above are completed, getting the response of the structure comes down to solving the system of Eq. 2.29.

### **2.4.3 Summary**

As introduced earlier, when modeling a problem utilising the FEM the selection of element type and properties is crucial in getting an accurate representation of reality. Additionally, it was described that selecting the mesh density and arrangement also impacts the accuracy of the solution. Developing better FE models involves some amount of trial and error regarding model optimisation. However, expertise on the physical problem as well as intuition regarding the expected results are undoubtedly important requirements.

### 3 Problem Definition

This section aims to offer a detailed description of the key parameters defining the reference problem studied in this work. Firstly, the problem geometry is described followed by the definition of the variable operational loads and damage states. Onwards, the proposed virtual sensor topologies are presented. Finally, details of the FE modelling, the source of the required data for this exploratory analysis, are discussed.

#### 3.1 Idealised Plate Domain

The highly complex structure of a ship poses a serious modelling and computational challenge for arithmetical simulations. Nevertheless, this complex design consists of simple structural entities such as plates and beams. The aforementioned structural elements have been studied in detail in the past century, hence there is plenty of knowledge built around the behaviour and modelling of such geometries. Ensuring the structural integrity of each individual component guarantees the safety of the structure as a whole. Consequently, a SHM system could also be focused at individual structural components.

The most common structural element on a ship is the stiffened panel, a typical arrangement of which is pictured in Figure 18. Albeit, for the purposes of this theoretical study, the geometrical domain was decided to be a rectangular (square)  $\alpha_0 \times \alpha_0$ -sized plate with a thickness of 1% its other principal dimensions. For simplification purposes, the value of  $\alpha_0$  is set to one meter. This idealised domain allows for a stripped-down theoretical approach to the quantitative influence of parameters such as sensor topology and damage severity on detection ability.

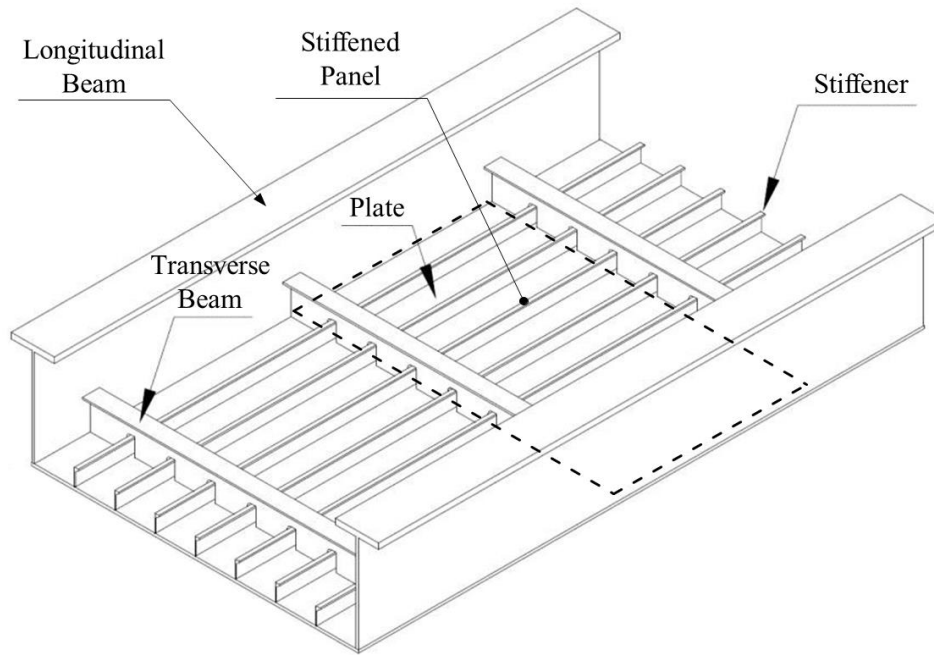


Figure 18. Typical structural arrangement of a ship's hull bottom. (Source: [38])

### 3.2 Operational Variability Definition

The plate was considered to be subjected to a variable operational pressure load. The load magnitude and its center location were modeled as random variables. The pressure profile is selected to be represented by the product of exponents of the quadratic relation of the centroid of a bell-shaped curve. The mathematical expression of the pressure profile is shown in Eq. 3.1.

$$q(x, y; Q_0, \bar{X}, \bar{Y}) = Q_0 \exp\left(-\frac{1}{2}\left(\frac{x - \bar{X}}{s}\right)^2\right) \exp\left(-\frac{1}{2}\left(\frac{y - \bar{Y}}{s}\right)^2\right) \quad \text{Eq. 3.1}$$

In the above,  $s$  is a deterministic shape parameter,  $x, y$  are deterministic variables representing coordinates on the plate plane relative to its center as depicted in Figure 19. Furthermore,  $\bar{X}, \bar{Y}, Q_0$  are independent continuous random variables following a normal distribution. More specifically,  $Q_0 \sim N(q_0; \mu_{Q_0}, \sigma_{Q_0})$  is the peak amplitude of the load, which will be referred to as load amplitude. The variables  $\bar{X} \sim N(\bar{x}; \mu_{\bar{x}}, \sigma_{\bar{x}})$ ,  $\bar{Y} \sim N(\bar{y}; \mu_{\bar{y}}, \sigma_{\bar{y}})$  represent the location of the peak of the load on the plate plane and will be referred to as load location. The particulars of each distribution were appropriately selected in order to achieve specific behaviour of the load. Namely, the parameters

of the load amplitude  $\mu_{Q_0}, \sigma_{Q_0}$  were selected such that the plate remains within the elastic regime and the load is distributed between zero and a maximum value. It was decided that the load random location would be symmetrically distributed around the center of the plate (0,0), which leads to  $\mu_{\bar{x}} = \mu_{\bar{y}} = 0$ .

The equation defining the load yields a symmetrical around its centre, bell-shaped surface that represents the load magnitude at each point. The surface extends to infinity along both axes of the plate plane. Due to the exponential nature of the distribution, the amplitude of the load degrades to zero in an asymptotic way within a relatively short distance from its centre. The significant part of the distribution, where non-zero amplitude is observed, is considered to be bound within a diameter extending six times the value of  $s$  around the center. The value of parameter  $s$  is set to be equal to  $\alpha_0/12$ . Hence, the resulting distribution of the load is constrained within a circular area with a diameter of  $\alpha_0/2$ , denoted with the red concentric circles in Figure 19. An indicative three-dimensional plot of the load profile around an arbitrarily selected center is presented in Figure 20.

Consequently, in order to fit the significant part of the load within the structural domain, its peak coordinates  $(\bar{X}, \bar{Y})$  had to be constrained within specified boundaries. Assuming that the range of  $(-3\sigma, +3\sigma)$  around the mean of each coordinate is equal to the range  $(-1/4\alpha_0, +1/4\alpha_0)$  on the plate, then the defined significant part of the load will fit completely within the structural domain with a probability of 99.46%. The latter is the product of the 99.73% probability of each independent coordinate value to be sampled within the specified range of  $6\sigma$ , according to the known theory for random variables following the normal distribution. Hence, the standard deviation of each coordinate was selected as  $\sigma_{\bar{x}} = \sigma_{\bar{y}} = \alpha_0/12$ .

Based on the aforementioned, it is concluded that the pressure distribution on the structural domain can be completely defined by its location and amplitude.

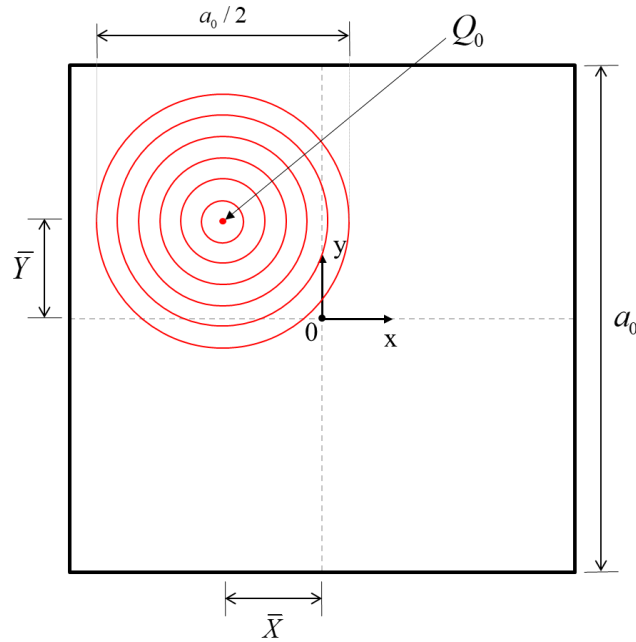


Figure 19. Top view of the plate with a two-dimensional representation of an instance of the load on it.

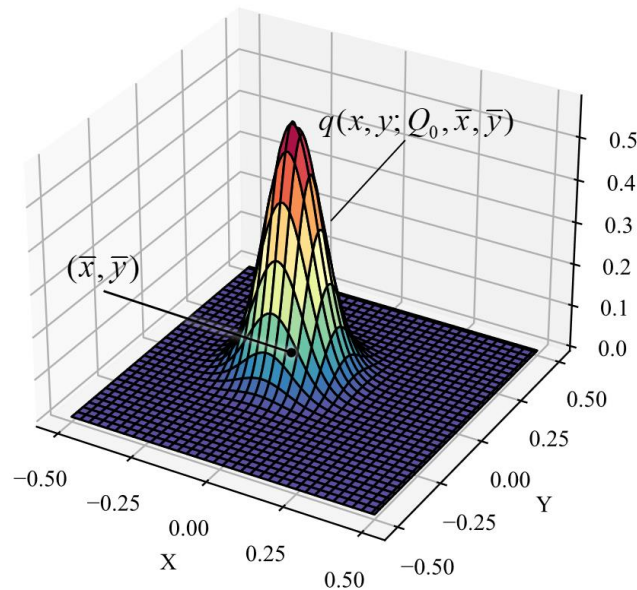


Figure 20. 3D representation of an indicative realisation of the load profile.

The properties described in the paragraphs above are visually summarised in Figure 21. The blue crosses correspond to a few thousand instances of sampled load locations. By design, 99.46 % of the load location samples should be corresponding to a point on the plate within the bounding box.

As long as the load's center is sampled within the bounding area, the entirety of the significant part of the load fits on the structural domain.

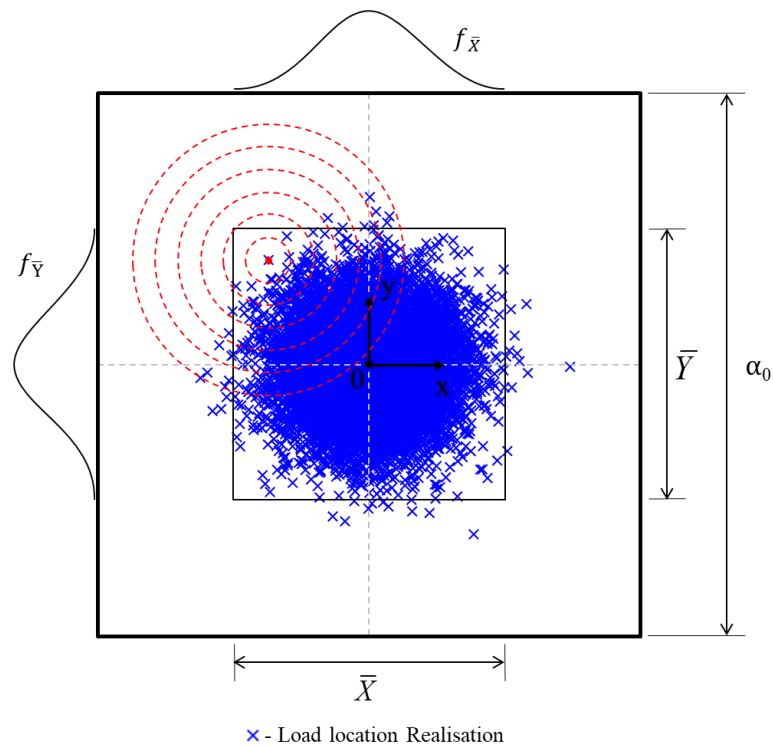


Figure 21. Visual representation of realisations of the load location.

Regarding the boundary conditions of the plate, it was decided that clamp supports would be simulated on all four edges of the plate, rendering all degrees of freedom bound along the edges.

### 3.3 Sensor topology

By the nature of the problem, there will always be a trade-off between the increased cost of implementing a high-fidelity local sensory arrangement and the reduced sensitivity of global sensing systems [7]. As a result, studying the effect of sensor density in the performance of the selected detection methods is of interest. This is believed to provide valuable insight to later be used for sensor placement optimisation.

In this work, strain measurements were analysed as the input signal for damage detection. Rectangular arrays of equally-spaced strain sensors were considered at four different grid densities. In particular, grids of 3x3, 4x4, 5x5 and 6x6 sensors were implemented in order to evaluate the



influence of sensor density on detection ability. The sensor layout on top of the plate is presented in Figure 22 for each of the selected sensor densities. Every sensor is represented by a gray square mark, while sensors are considered to measure both longitudinal strain components along  $x$  and  $y$  axis ( $\varepsilon_x, \varepsilon_y$ ), as well as the in-plane shear strain ( $\varepsilon_{xy}$ ) on the plate at the specified location.

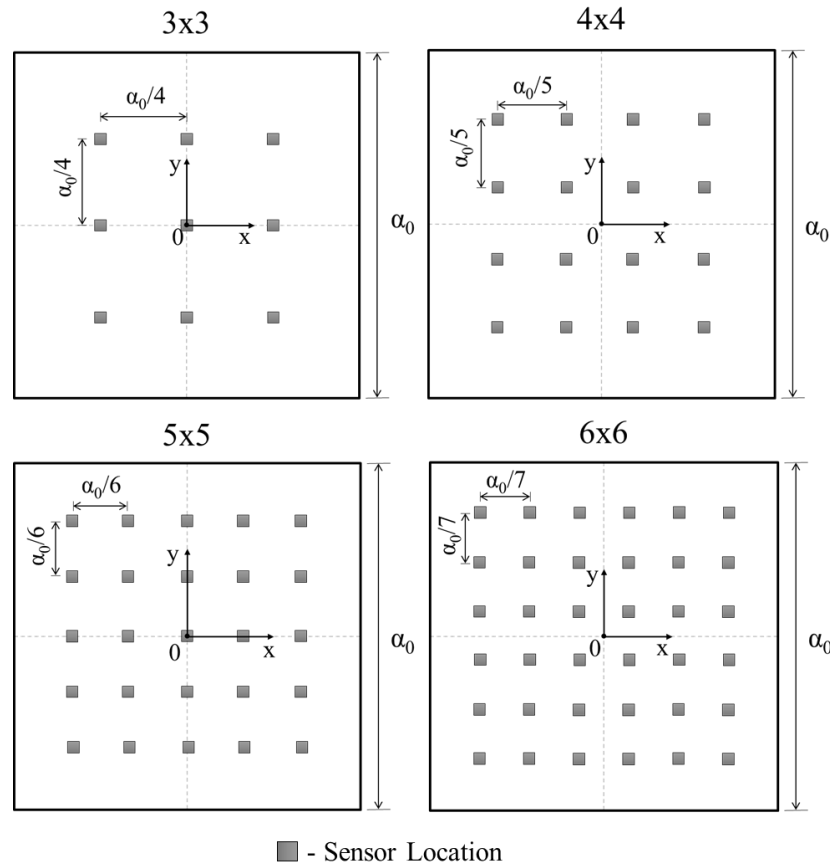


Figure 22. Sensor topology overview. Each sensor measures longitudinal strain components along  $x$  and  $y$  axis as well as the in-plane shear strain on the plate.

### 3.4 Damage introduction

The meaning of damage can vary widely depending on the approach and the purpose of each analysis. In this study, the damage was modeled as various levels and extents of uniformly reduced plate thickness. In particular, two categories of damage scenarios were introduced. The first concerned global damage affecting the entire domain while the other included locally contained cases. It is quite obvious that the global thickness loss can be thought of as a direct model of

uniform corrosion. The localised thickness loss, on the other hand, could be viewed as an abstract, fictitious model equivalent to the real-world pitting corrosion.

On a closer look at the modeling of damage for the purposes of this analysis, in the case of the entirely damaged domain, the only parameter used to completely specify the damage was the remaining thickness as a percentage of the nominal thickness. On the contrary, in the case of the localised damage, the additional parameters of its center coordinates and its area of extent were introduced as well.

Particularly, the size of the area of the localised damage was considered fixed and was modeled as a rectangular subsection of the plate. For the purpose of accommodating FE modeling, which is discussed in more detail in Section 3.5 below, the damaged area was sized as a whole multiple of elements from the FE model, more specifically as a 3x3-element wide square area. Regarding the location of the local damage, the co-ordinates of the center of the damaged area  $(X_d, Y_d)$  were modeled as random variables following the normal distribution,  $X_d \sim N(x_d; \mu_{X_d}, \sigma_{X_d})$ ,  $Y_d \sim N(y_d; \mu_{Y_d}, \sigma_{Y_d})$ , with  $\mu_{X_d} = \mu_{Y_d} = 0$ ,  $\sigma_{X_d} = \sigma_{Y_d} = \alpha_0 / \sqrt{12}$ . The statistical parameters were selected this way so that 99.46% of the sampled damaged areas fit completely within the plate. The samples of the co-ordinates were generated with the Latin Hypercube Sampling (LHS) method that will be described on a succeeding section. The sampled coordinates were quantised so that the damaged area would always be aligned with the FE mesh, once again for the purpose of simplifying FE modeling. Additionally, the samples were filtered appropriately so the entire damaged area would always fit completely within the model. Damage was taken into account in the FE model by appropriately reducing the thickness of the affected elements.

It was considered that the aforementioned damage models represent two commonly occurring damage types in marine structures that induce material loss. This loss directly influences the stiffness of the structure which causes a direct disturbance in the strain field at and around the damaged area. It is believed that this disturbance bares valuable information and can be used as the core input signal for a strain-based SHM system.

### 3.5 Finite Element Modeling

On the basis that the thickness of the plate was considerably smaller than its other dimensions, it was modeled using four-node rectangular shell elements with six degrees of freedom at each node; three translations along an orthogonal axis system and the respective rotations about these axes.

Element size was determined by comparing relative solution accuracy between alternative reasonably sized mesh options in three indicative load cases. All load scenarios were attributed the maximum peak magnitude and were centered at the center of the plate (0,0), the furthest possible away from the center  $(\bar{X}_{max}, \bar{Y}_{max}) = (\alpha_0/4, \alpha_0/4)$  and halfway in between. The mesh size was controlled by the element edge length. The finest mesh was formed by elements with an edge size of 0.01 m, which constitutes 0.1% of the total plate area to be meshed. A few more meshes with incrementally increasing size of element edge were also submitted to solution for comparison. Taking into account the highly variable pressure profile, this magnitude of discretisation is considered reasonable.

The sensor locations at which solution data were acquired were defined by an equally spaced 3x3, 4x4, 5x5 and 6x6 array of coordinates accordingly. For every mesh size the longitudinal components of the strains and the in-plane shear component ( $\varepsilon_x$ ,  $\varepsilon_y$  and  $\varepsilon_{xy}$ ) as well as the maximum deflection perpendicular to the plate plane ( $U_z$ ) were extracted at every sensor location for each load case. The value ( $R_{i,j}$ ) of the absolute differences between corresponding measurements ( $X_{i,j}$ ) from every mesh size ( $j$ ) as a percentage of the relevant measurement in the finest mesh scenario ( $j=1$ ) were calculated as per Eq. 3.2, where  $X$  refers to either a strain measurement or the maximum deflection measurement.

$$R_{i,j} = \frac{|X_{i,j} - X_{i,1}|}{|X_{i,1}|} \quad \text{Eq. 3.2}$$

Statistical analysis of the aforementioned acquired values was implemented in order to justify the selection of the largest mesh size that produces adequate solution accuracy, in order to optimise the process with respect to solution times. The mean, standard deviation and coefficient of variation of these relative differences is calculated. These metrics are visually summarised in Figure 23 and Figure 25.

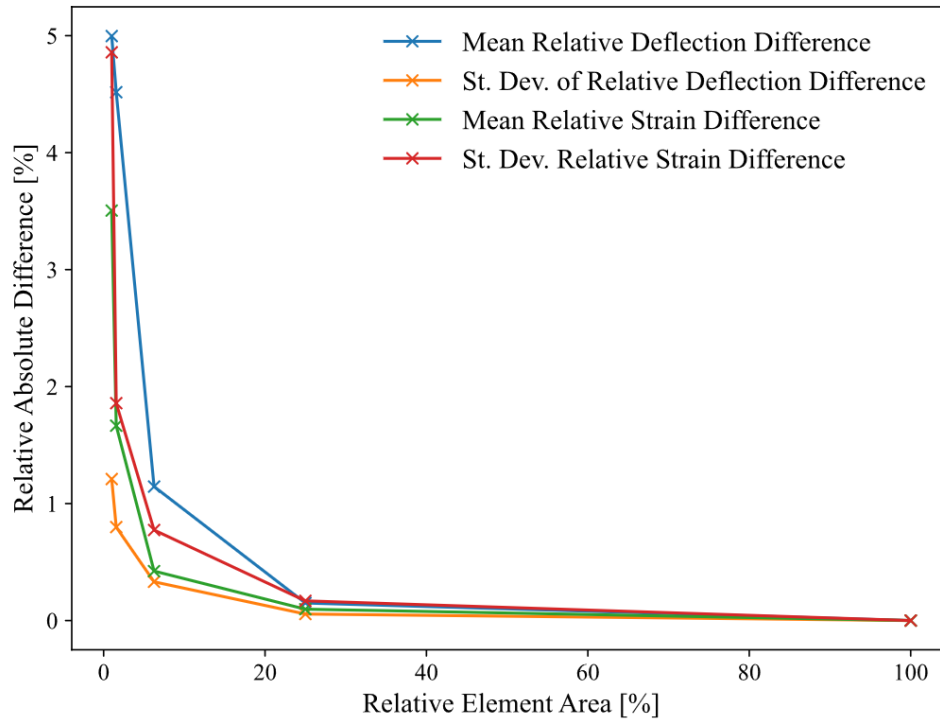


Figure 23. Mean and standard deviation of relative absolute differences between measurements plotted against element size as a percentage of the finest element.

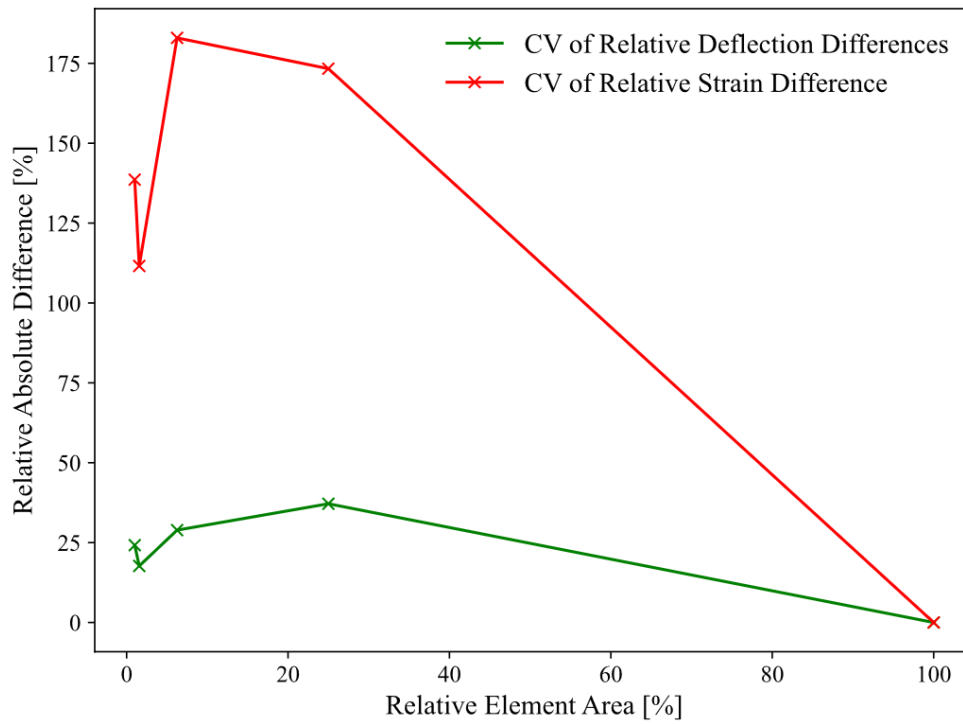


Figure 24. Coefficient of Variation (CV) of relative absolute differences between measurements plotted against element size as a percentage of the finest element.

The relative element area refers to the ratio of the finest element area over each subject element area. The selected element edge sizes for comparison were 0.1, 0.04 and 0.02 m. In light of the above comparative exploration, it was considered safe to assume that solution accuracy with respect to mesh size has adequately converged by the 0.02 element edge case. On this account, an element width of 0.02 m was selected for the FE model provided that it offered sufficient solution accuracy and at the same time would save in required simulation time. As a result, a 50x50-element structured mesh was developed to simulate the rectangular plate. The meshed plate is presented in Figure 25.

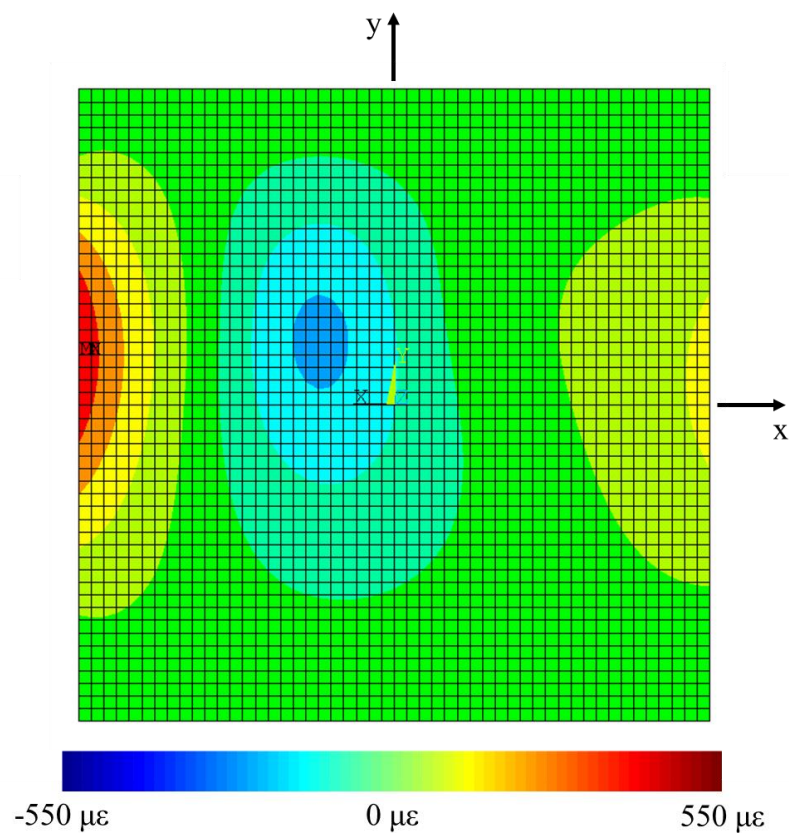


Figure 25. Meshed plate and contour plot of the longitudinal ( $\epsilon_x$ ) strain component on the face of the plate for an indicative pressure load realisation.

Concerning the boundary conditions, all degrees of freedom of the nodes along the edges of the plate were restricted to simulate clamped support conditions. The distributed load was applied by discretising the continuous function that controls its profile. For each load case, the corresponding values of the load magnitude were acquired at the locations of the nodes. More specifically, the corresponding value of the load ( $q$ ) at a specific node with coordinates  $(x_n, y_n)$ , under the

given loading scenario  $(Q_0^{(r)}, \bar{X}^{(r)}, \bar{Y}^{(r)})$  is calculated as  $q(x_n, y_n; Q_0^{(r)}, \bar{X}^{(r)}, \bar{Y}^{(r)})$  in accordance with Eq. 3.1.

The FE model was repeatedly solved for  $10^4$  randomly sampled realisations of the input load for each of the damage scenarios and each of the sensor grid arrangements. The simulations were automated to repeat with different input parameters each time. The contour plot of the longitudinal strain component ( $\varepsilon_x$ ) on the face of the plate occurring from one indicative solution is also pictured in Figure 25.

## 4 Exploratory Data Analysis

Before proceeding to the central topic of the present study, the application and evaluation of the classification methods, it is considered important to discuss in more detail about the structure of the acquired datasets, elaborate on any preprocessing that may have been applied and provide some initial insight on the data that will prove useful in drawing conclusions and understanding certain behaviours of the detectors.

### 4.1 Dataset Construction

In order to draw reliable conclusions about the performance of the statistical pattern recognition methods of interest on the specified problem, gathering a large set of representative data was necessary. Because of the scale of the required data and the modeling of the problem, real-world model experiments were rendered impractical, hence the required information were gathered through numerical approximations of virtual experiments, as explained in the previous section. The data sets were obtained from iterative solutions of the FE model for different realisations of the input parameters. These random parameters included the pair of coordinates representing the load peak location and the one controlling the load magnitude, as introduced earlier. In the case of the localised damage, the coordinates of the center of the damaged area were also introduced as random input parameters.

The random parameters were sampled using the Latin Hypercube Sampling (LHS) method [39]. The LHS method promises to recreate a given distribution with less samples than alternative sampling methods. The basic idea of LHS is the stratification of the cumulative distribution function (CDF) of the distribution of interest in equiprobable sections and the selection of one random sample in each stratum.

Each of the three measured strain components at each sensor location was considered a feature. A feature vector consists of a set of measurements of one or more given features occurring from the repetitive solutions of the FEA problem with different realisations of the random input parameters.

The number of simulations was decided to be ten thousand to ensure convergence, which was verified by calculating the differences of the mean of each feature vector between two sets of

randomly sampled input data. The statistical distribution of these differences is plotted in Figure 26, where it is observed that the differences are distributed around near-zero values confirming adequate convergence.

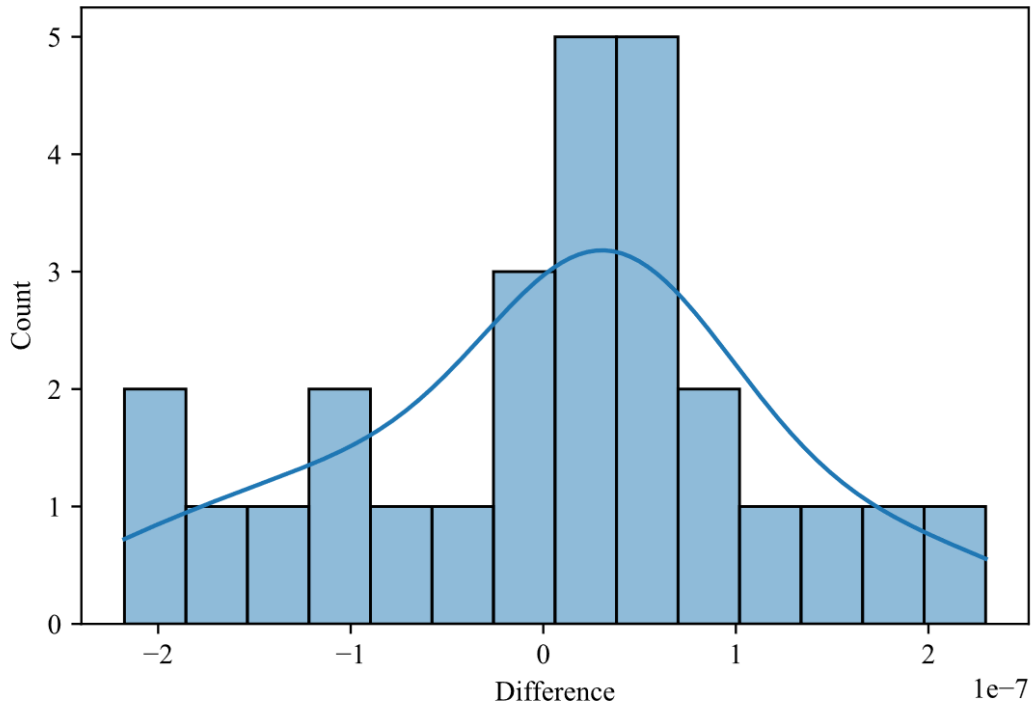


Figure 26. Distribution of differences, in absolute strain units, between mean strain features of two feature vectors.

As implied earlier, the collected data from each virtual experiment are essentially  $10^4$  strain measurements for each of  $3n^2$  features, where  $n$  is the number of sensors in an  $n \times n$  sensor arrangement option. The overall concept is to study the ability of the different classification algorithms to identify the existence of corrosion based on the strain response of the plate. In order to test the classification algorithms, the input data should adequately represent both of the classes of interest. As a result, the feature vectors submitted to the detectors consisted of  $2 \times 10^4$  measurements, half generated by simulating the healthy plate FE model and the other half from a damaged plate at a given uniformly reduced thickness or a locally contained uniform thickness reduction at random locations on the plate. The data are labeled appropriately to identify the state of the plate from which they occurred in order to validate and measure the performance of the detectors, quantifying it in terms of probability of detection and probability of false alarm.



The mathematical framework for both the statistical classifiers and the neural network requires a calibration process, referred to as training, before they can be applied for data analysis. During this process, known input-output sets of data are iteratively processed by the detectors, each time applying an optimisation algorithm to fine-tune several parameters. This process is intended to produce a set of parameters such that the occurring detector is able to generalise and to accurately classify new, unknown data. In an intuitive, simplified view, every detector in the beginning can be thought of as a set of malleable, yet unshaped moulds. Each of these moulds is repeatedly exposed to known instances of a corresponding class, gradually acquiring the shape of the prominent characteristics of instances within the aforementioned class. Provided the moulds are exposed to adequate, representative instances of each class, the final set of moulds can be used to classify uncharted data.

As a result of the explanation above, the need for fully labelled sets of data for training the classification methods is made apparent. It should also be noted that the aforementioned set of data is not suitable for use as a testing set to measure the performance of the classifiers. It is of utmost importance that the data used to evaluate the performance of every detector are never fed to the detector before during training, otherwise the acquired performance metrics cannot be considered reliable. In this regard, the formed datasets of  $2 \times 10^4$  measurements, consisting of 50% of data occurring from solutions of the healthy plate and 50% occurring from damaged plate scenarios, are split in two subsets in a random way. 70% of the initial set ( $1.4 \times 10^4$  instances) forms the training data set and the remaining 30% ( $0.6 \times 10^4$  instances) constitutes the testing data set.

## 4.2 Data Preprocessing

### 4.2.1 Statistical Patterns of the Strain Response

Upon collecting the strain data from the simulations, an initial statistical exploration was performed to gain insight on the strain response of the plate. To keep the presentation of the results within reasonable extent, a few indicative features were selected, representative of the overall problem. Specifically, in the case of the 3x3-sensor grid arrangement, a visual representation of which can be viewed in Figure 22, each of the three measured strain components are selected for the top left, middle top and central sensor (referred to as sensors 1, 2 and 5 respectively). This selection of sensors is representative of the strain response of the entire plate due to the symmetry

of the selection around the center of the plate as well as the fact that the ten thousand sampled loading scenarios adequately represent the sampling space. The strain response is investigated for both the healthy state and one damaged state. In particular, the selected damage scenario is a uniformly corroded plate at 50% the nominal thickness. Figure 27 contains indicative probability plots of one feature for each of the healthy and damaged states against a fitted normal distribution. They, also, contain comparative histograms between the two states for the same feature. It was observed that most features are adequately represented by a normal distribution while some may diverge at the tail ends.

For a more specific look into the statistical structure of the strain response of the plate, Figure 28 through Figure 30 each depict the scatterplot matrix of all three features at the selected sensor locations mentioned above, comparing the healthy and damaged scenarios. The diagonal subplots contain the univariate histograms of each strain component. The upper triangle plots depict scatterplots in pairs. The bottom triangle subplots contain contour lines of the kernel density estimates in pairs of strain components. Orange-coloured items represent the healthy state, spanning at a relatively contained strain range, directly proportional to the load magnitude. On the other hand, blue-coloured items represent the damaged state, spanning at greater strain range, being influenced simultaneously by the load magnitude and the reduced thickness. It is observed that the measurements from both classes significantly overlap. No apparent distinction between data from the healthy and damaged state is noticed.

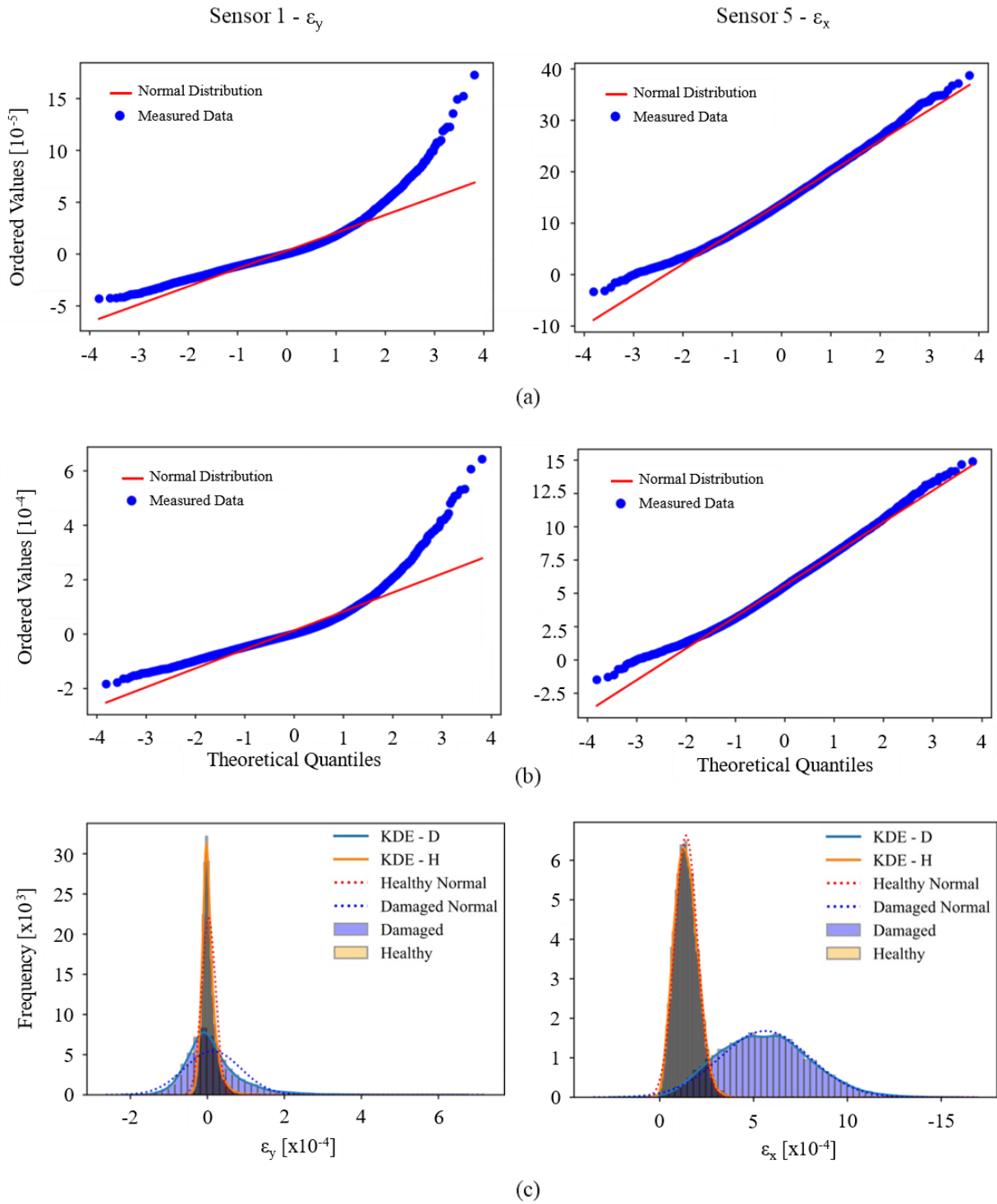


Figure 27. Indicative probability plots for (a) the healthy state, (b) damaged state and (c) comparative histograms between strain components at healthy and damaged state at corresponding sensor locations.

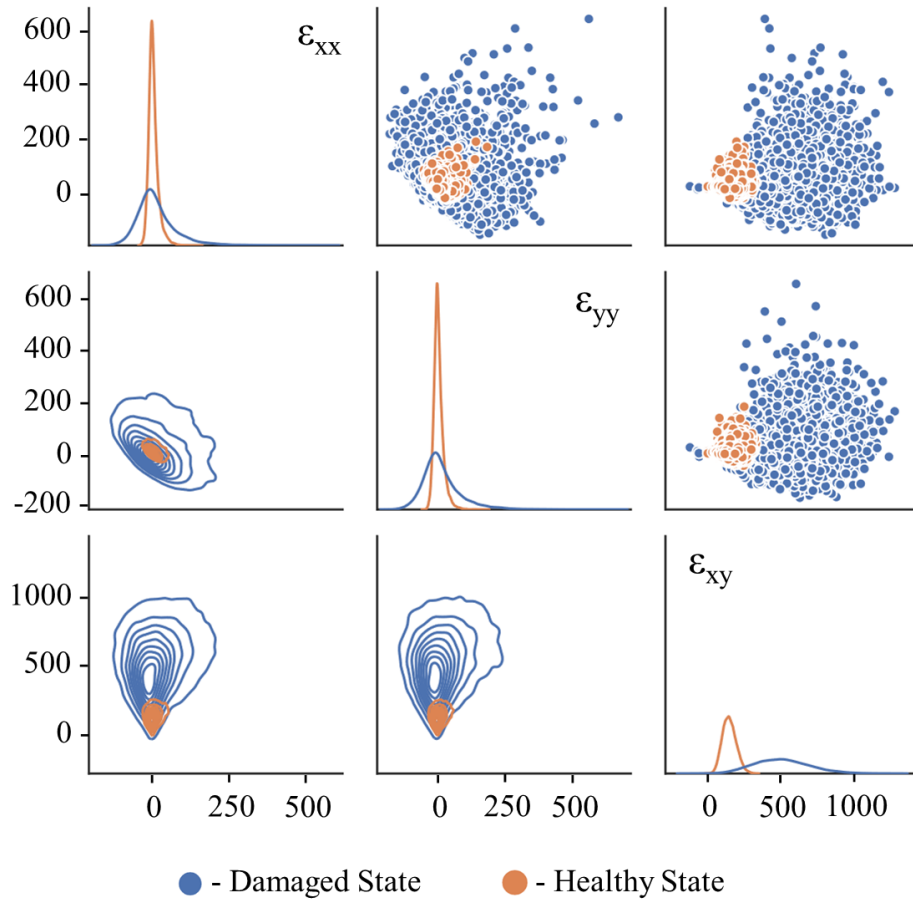


Figure 28. Scatterplot matrix of the strains at Sensor 1 (3x3 grid, upper left corner).

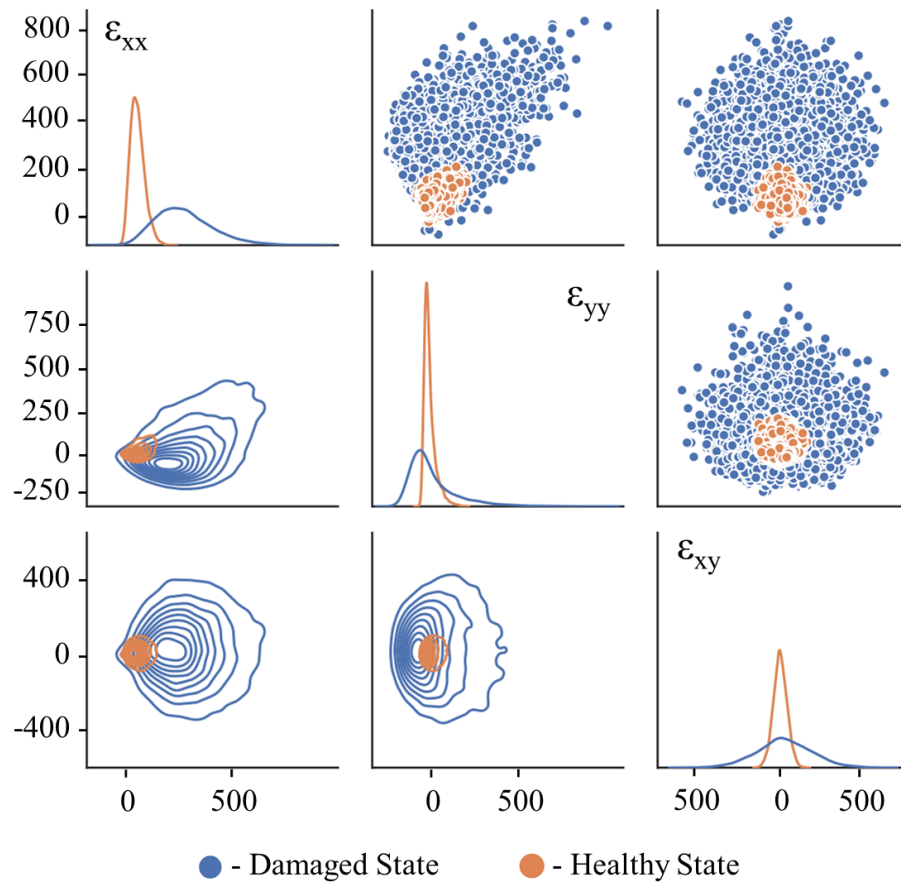


Figure 29. Scatterplot matrix of the strains at Sensor 2 (3x3 grid, middle-top).

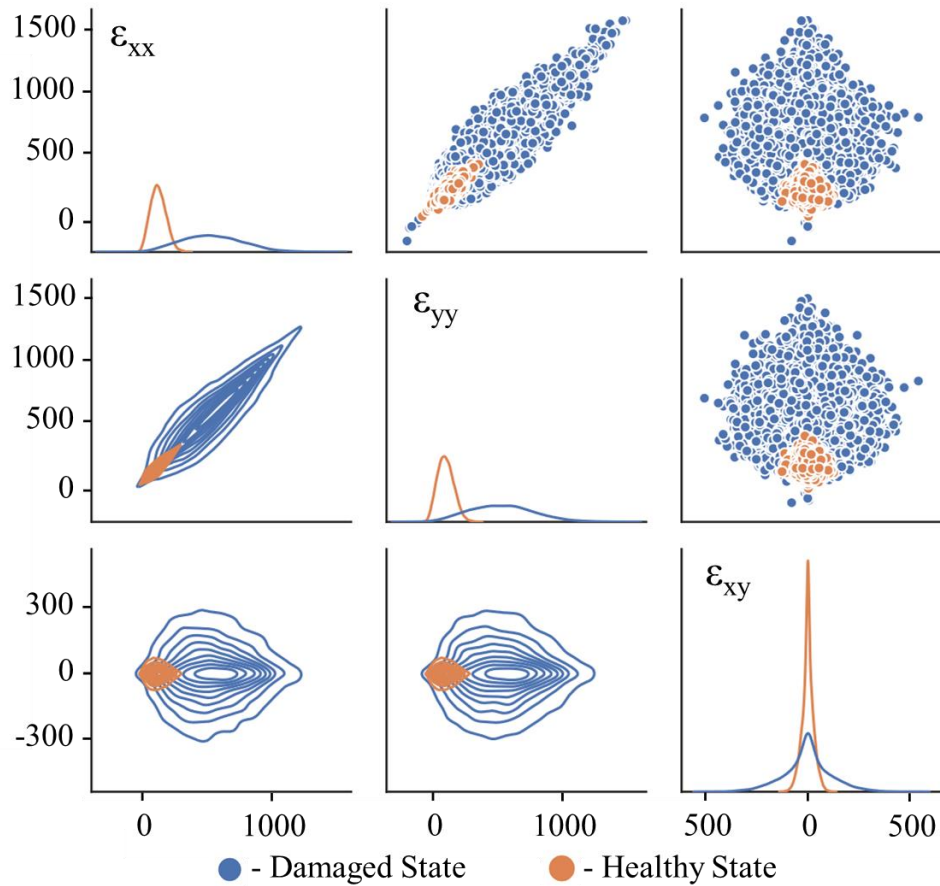


Figure 30. Scatterplot matrix of the strains at Sensor 5 (3x3 grid, central).

Another observation that is noteworthy is that when comparing strains from the healthy and damaged case in which the thickness is uniformly halved, the average of the ratios of the mean strains converges to the value of four. Plate theory [40] predicts that normal strains induced from plate bending are inversely proportional to the squared thickness of the plate. Therefore, the above noted result falls in line with plate theory, validating the modeling in this work.

#### 4.2.2 PCA of the Input Vectors

In data analysis, it is common to pursue dimensionality reduction of the raw collected data by concentrating valuable information in a subset of the initial data or a downsized, transformed new set that is extracted using statistical tools on the original data [41]. Keeping in mind that in the present study the number of selected features is relatively limited, having a maximum of 108 features in the 6x6 sensor case, in tandem with the fairly short number of measurements for each

feature in a dataset, the full feature vector could be submitted to analysis as well, without significant computational power and time requirements. Considering that this is an exploratory approach and that in a practical application the data would likely be of much larger extent, vectors obtained via dimensionality reduction were submitted to analysis in order to investigate the performance of the detectors on such data and compare it against that of the full vector input scenario for additional insight. Therefore, Principal Components Analysis (PCA) [42] was used to reduce the dimension of the feature vector. By analysing the resulting vectors, it was observed that the first two principal components retain about 60% of the set's variation for the 3x3 grid and 78% of the set's variation for the rest of the sensor grid options. Figure 31 visually presents the explained variation per principal component for all sensor grid cases. Every subplot corresponds to data extracted using a different virtual sensor grid arrangement. In each subplot, a given bin represents the percentage of variance retained by the respective principal component. As discussed in Section 2.2, because of the way PCA is structured, the bins are bound to appear in decreasing order, with every following principal component containing less variance in the information.

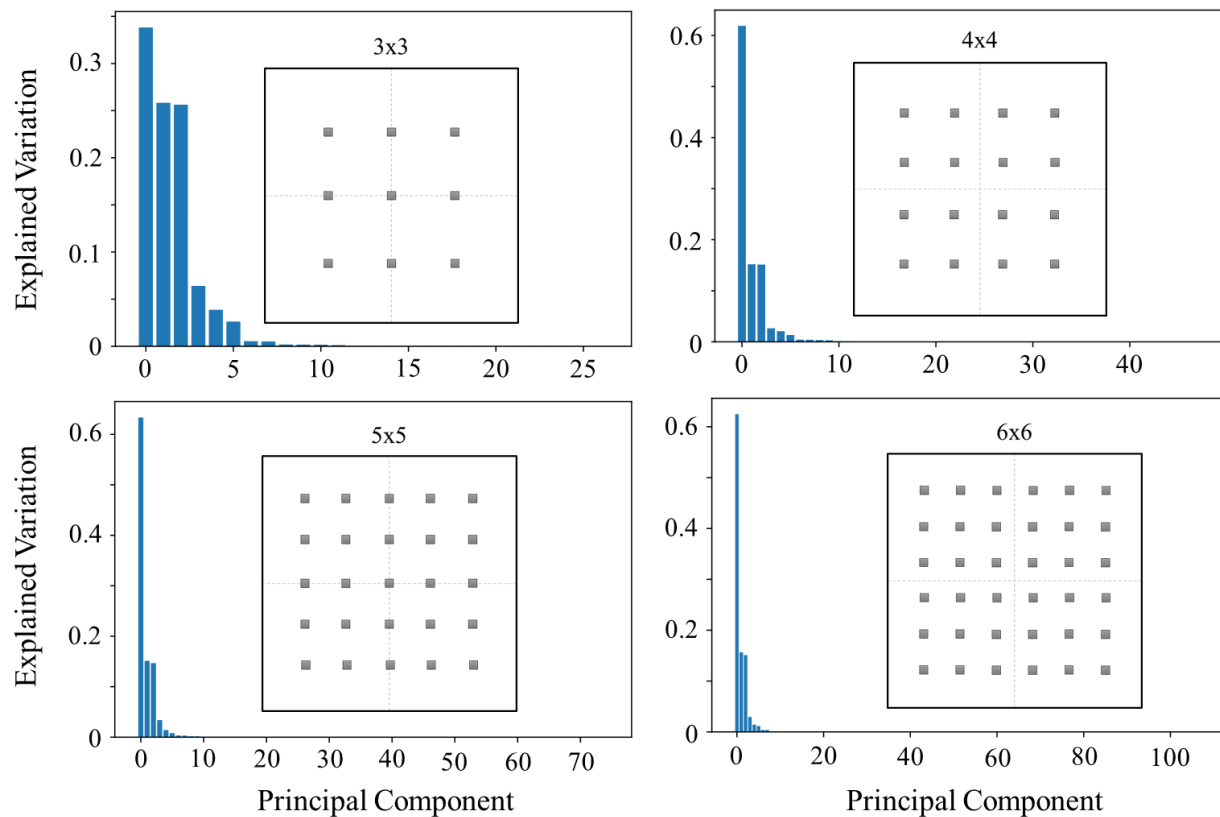


Figure 31. Explained variation retained in each principal component of a vector composed of one healthy and a damaged case in all sensor grid scenarios.

Figure 32 presents an indicative scatterplot in pairs for the first two principal components of a healthy and a uniformly damaged case at 50% nominal thickness with data acquired using the 6x6 sensor layout. It is observed that healthy and damaged state data remain clustered with significant overlap, with the latter showcasing significantly higher variance. The same statistical behaviour was detected in the raw strain measurements, indicative scatterplots of which were earlier presented in Figure 28 through Figure 30. Albeit using the 3x3 virtual sensor grid positions of measurements in the latter, the overall statistical behaviour of strains is not expected to be influenced by slightly changing the position of measurements provided the sampling space has been represented adequately, which was verified in Section 4.1. Taking into account all the above, in the present problem, patterns in the data appear to be retained after PCA. As a result, even though PCA is expected to produce separable clusters, it appears that in the particular modeling, it is still difficult to discriminate between the classes even in a principal component projection of the data. Consequently, using the reduced vector as input to the detectors is not expected to yield significant performance impact.

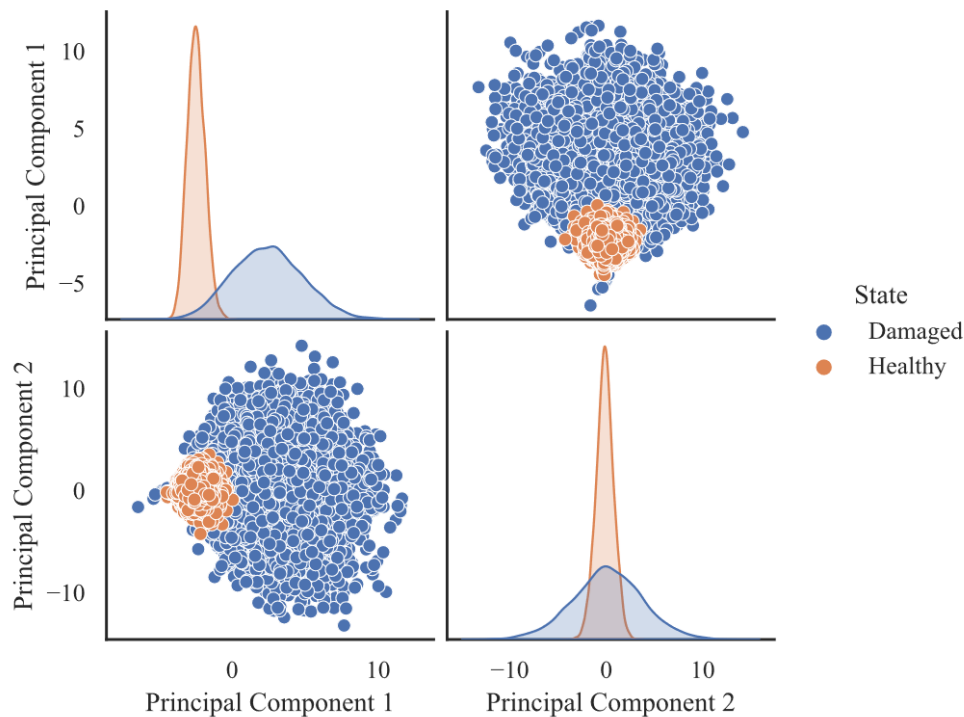


Figure 32. Comparative pairplot of the first two principal components of healthy and damaged 50% nominal thickness) cases using the 6x6 sensor grid.



## 5 Results and discussion

In the previous sections the way datasets were formulated and preprocessed was discussed. Once the information was prepared appropriately, it could be submitted to the classifiers for further processing. For exploratory purposes, the following feature vectors were used as input to the detectors:

- A univariate feature vector consisting of the first principal component of the strain data.
- A bivariate feature vector consisting of the first two principal components of the strain data.
- The entire multivariate feature vector consisting of  $3 \times n \times n$  strain measurements.

A realisation of the feature vector is symbolised as  $\boldsymbol{\varepsilon}_i$ .

### 5.1 Formulation of the Detectors

The mathematical framework regarding the classification methods of interest has been presented in Section 2.1. In those paragraphs, the general form of the methods was discussed. Herein, some unspecified parameters that were introduced in the aforementioned equations on the theoretical level will be formally determined, forming the final classifiers used in this study.

In light of the initial statistical exploration of the acquired data presented in Section 4.2.1, the normal distribution was considered a suitable model as a statistical basis for the employed detectors. The assumed statistical model is necessary to estimate the various parameters required for the implementation of the aforementioned classifier methods.

For the binary classification problem at hand, the notation used for the two classes was the letter “ $H$ ” representing the healthy state (non-existence of damage) and the letter “ $D$ ” damaged state (existence of damage). The prior probabilities for the two classes were considered equiprobable and were symbolised as  $p_H = p(H)$  and  $p_D = p(D)$  accordingly, hence  $p_H = p_D$ . The normal probability density function (PDF) of each class  $j$  was referred to as  $f_j(\boldsymbol{x})$  at a given vector  $\boldsymbol{x}$ . For the multivariate normal distribution, the formula of the PDF is:

$$f_j(\mathbf{x}) = \frac{1}{\sqrt{(2\pi)^k |\boldsymbol{\Sigma}_j|}} \exp\left(-\frac{1}{2}(\mathbf{x} - \boldsymbol{\mu}_j)^T \boldsymbol{\Sigma}_j^{-1}(\mathbf{x} - \boldsymbol{\mu}_j)\right) \quad \text{Eq. 5.1}$$

where  $k$  is the length of vector  $\mathbf{x}$ ,  $\boldsymbol{\mu}_j$  is the mean vector and  $\boldsymbol{\Sigma}_j$  is the covariance matrix of class  $j$ .

### 5.1.1 Likelihood Ratio Test

For the LRT, in section 2.1.1 it was explained that the classification decision is made based on the ratio of the class-conditioned PDFs of the measurements combined with a decided threshold. In absence of a formal reason for a biased classification, the threshold was set to unity. Summarising, taking into account the introduced notation the decision rule is reformed as:

$$\begin{cases} \text{If } \gamma_i = \frac{p(\boldsymbol{\varepsilon}_i|H)}{p(\boldsymbol{\varepsilon}_i|D)} > 1 \Rightarrow \text{Healthy} \\ \text{If } \gamma_i = \frac{p(\boldsymbol{\varepsilon}_i|H)}{p(\boldsymbol{\varepsilon}_i|D)} < 1 \Rightarrow \text{Damaged} \end{cases} \quad \text{Eq. 5.2}$$

### 5.1.2 Discordant Outlier Analysis

As introduced in section 2.1.2, the discordant outlier method requires the choice of a class as basis. In this study, the class of choice was the healthy state. Thus, in this approach, the measured vector was classified as healthy or damaged depending on distance between that measurement and the center of the healthy state data distribution. The fitting distribution, as explained earlier, was the normal distribution.

For the univariate feature vector, the value of the inverse CDF of the standardised normal distribution at  $\alpha = 99\%$  confidence,  $\Phi^{-1}(0.99) = 2.326$ , was selected as a classification threshold, leading to the following decision rule:

$$\begin{cases} \text{if } z_i < \Phi^{-1}(0.99) \Rightarrow \text{Healthy} \\ \text{if } z_i > \Phi^{-1}(0.99) \Rightarrow \text{Damaged} \end{cases} \quad \text{Eq. 5.3}$$

On the same basis, for the univariate feature vector, the value of the inverse CDF of the chi-squared for  $k$  degrees of freedom  $\Psi(\alpha, k)$  at  $\alpha = 0.99$  probability, was set as the threshold. The final decision rule is stated as follows:

$$\begin{cases} \text{if } d_M^2 < \Psi(0.99, k) \Rightarrow \text{Healthy} \\ \text{if } d_M^2 > \Psi(0.99, k) \Rightarrow \text{Damaged} \end{cases} \quad \text{Eq. 5.4}$$

### 5.1.3 Quadratic Discriminant Analysis

In the case of QDA, as discussed in section 2.1.3, the use of the normal distribution is inherently modeled within the detector framework. For the problem at hand, where equiprobable priors were considered as mentioned above, the last logarithmic term in Eq. 2.15 would be zeroed out. The notation in the latter equation falls in line with the one introduced in this section and describes the specific problem addressed in this study. As a result, the decision rule can be written as:

$$\begin{cases} \text{if } \delta_Q(\boldsymbol{\varepsilon}_i) < 0 \Rightarrow \text{Healthy} \\ \text{if } \delta_Q(\boldsymbol{\varepsilon}_i) > 0 \Rightarrow \text{Damaged} \end{cases} \quad \text{Eq. 5.5}$$

## 5.2 Detection metrics

Once the underlying mathematical framework of the classification methods has been laid out, the subsequent step is to fit the detectors using the training datasets. The test datasets can then be processed by the fitted detectors and the results can be evaluated.

An important factor in the acceptance of SPR for SHM in the industry is the standardisation of reliable performance evaluation metric [19]. In the particular work, the detection ability of the SPR methods presented earlier was quantified by applying these methods on test data and measuring the ratios defined below based on the returned predictions. Provided that the available data were produced by FEA simulations and are clearly, indisputably classified, accompanied with the relevant metadata, the employed metrics were deemed sufficient and representative for the theoretical exploration and comparison of each detector's performance. The metrics used were a) the Probability of Detection (POD) defined as the ratio of correctly predicted damaged instances over total damaged instances (Eq. 5.6) and b) the False Alarm Rate (FAR) defined as the ratio of falsely predicted damaged instances over total healthy instances (Eq. 5.7).

$$\text{POD} = \frac{\# \text{ Correctly predicted damaged instances}}{\# \text{ Total damaged instances}} \quad \text{Eq. 5.6}$$

$$\text{FAR} = \frac{\# \text{ Falsely predicted damaged instances}}{\# \text{ Total healthy instances}} \quad \text{Eq. 5.7}$$

### 5.3 Detection of uniform corrosion

Initially, the detectors were evaluated on their ability to identify uniform thickness reduction across the entire domain. The POD and FAR were calculated for each detector, for all sensor grid densities, all the different input vectors and were tracked across different damage severity scenarios. The damage severity is represented by thickness wastage, the percentage of lost thickness over the nominal plate thickness. The above is visually summarised in the graphs of Figure 33. Each plot compares the performance of one method for the given input vector and different sensor grid arrangements. The area below 50% POD, where essentially there is no point in discussing a detector, is greyed out. The subplots are grouped by employed detector (rows) and input vector (columns).

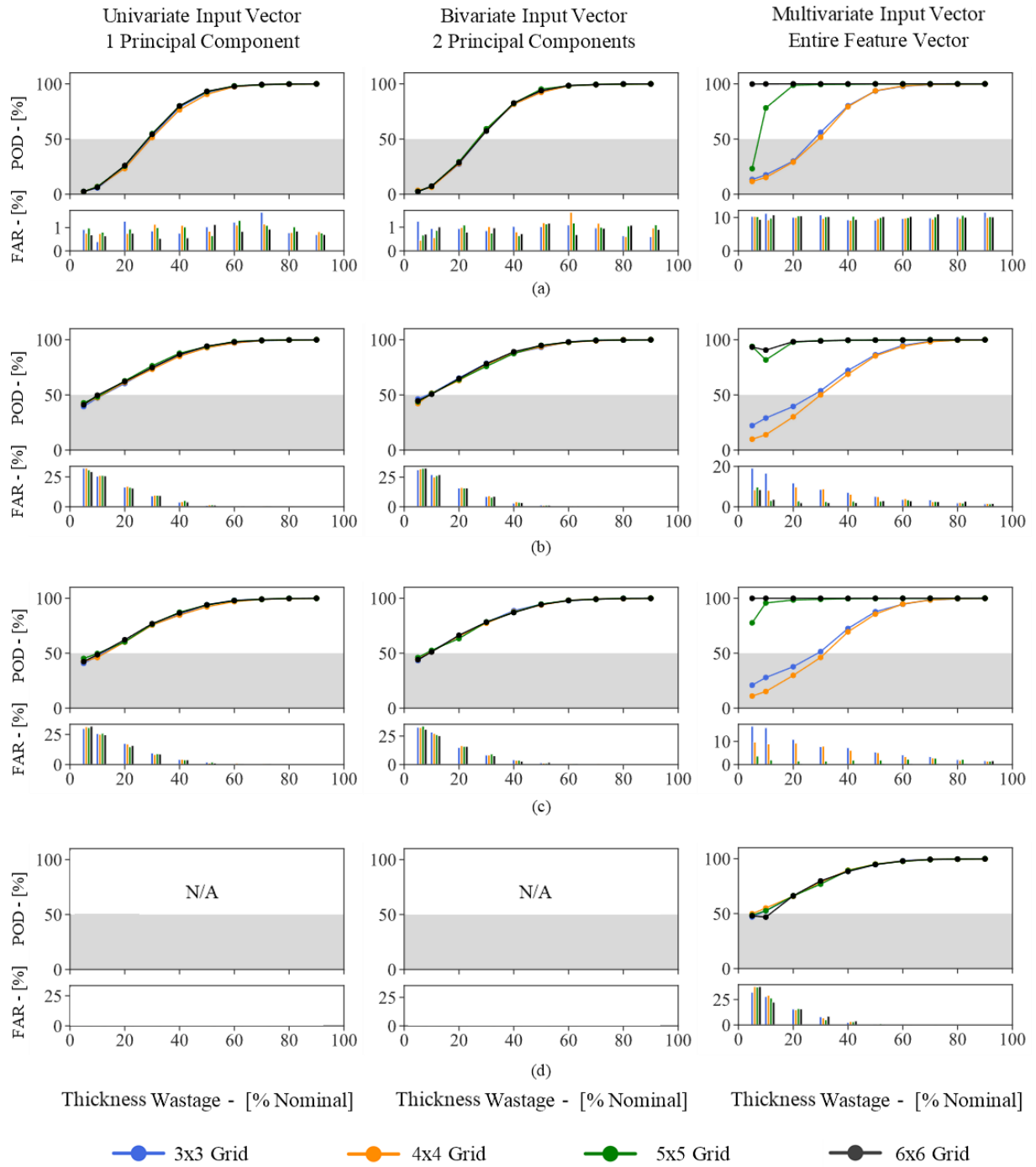


Figure 33. POD and FAR plot against thickness wastage percentage for different input vector cases and regarding (a) Discordant Outlier Analysis, (b) Likelihood Ratio Test, (c) Quadratic Discriminant Analysis and (d) ANN.

Similarly, the graphs of the POD and FAR are plotted against thickness wastage, this time directly comparing between detectors for a given input feature vector and sensor density. The subplots are grouped by grid case detector (rows) and input vector (columns).

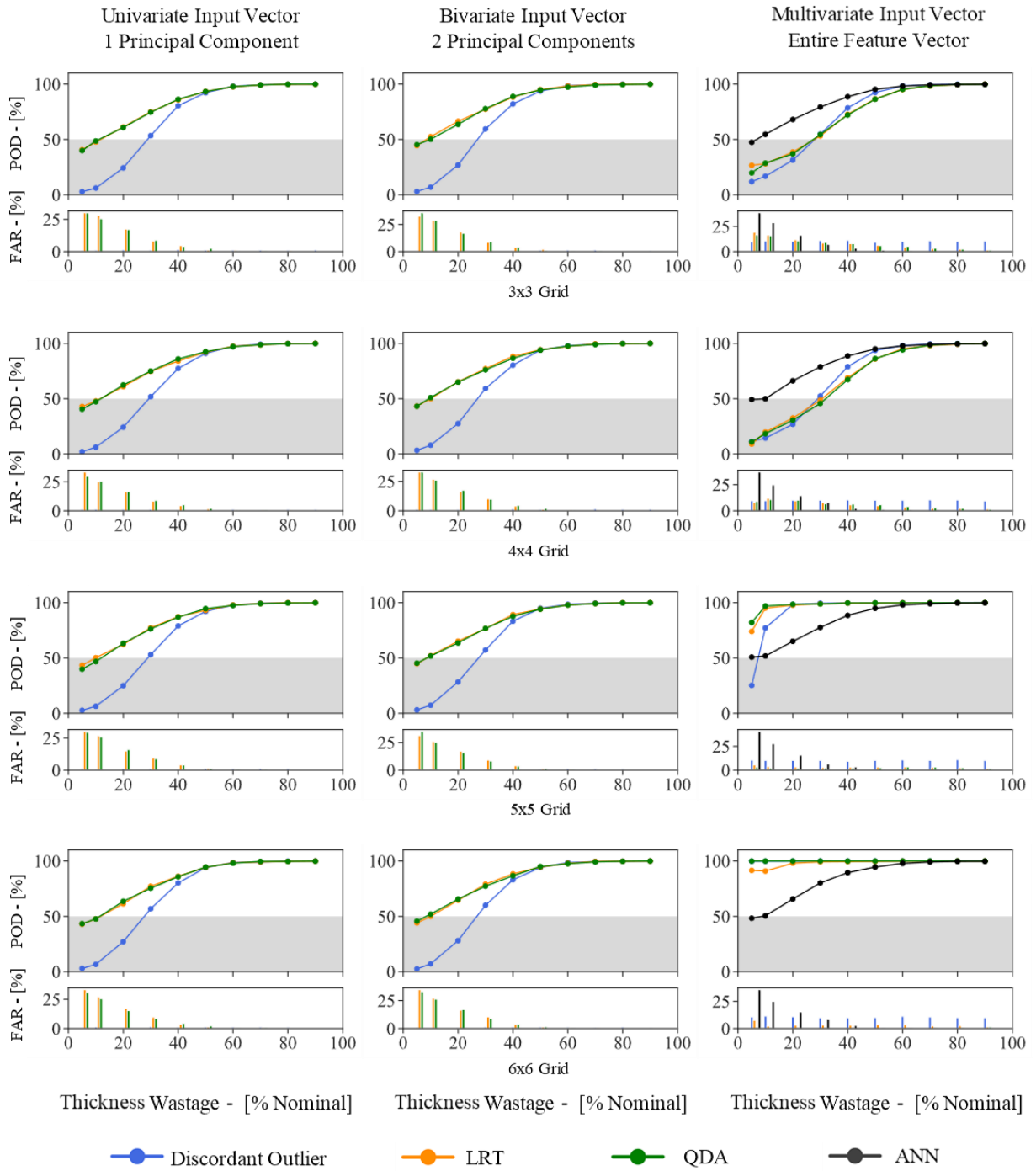


Figure 34. POD and FAR plot against thickness wastage percentage for different input vector cases and sensor grid cases.

Taking into account all available results, it is observed that when PCA is applied to the input vector, the POD and FAR seem to not be affected by the sensor grid. In the present work, while the raw input vector dimension increased, at most the two first principal components were kept for analysis. The aforementioned behavior implies that the first principal components capture the same information content from the expanding feature vector. Hence, in the particular problem, the lower-dimensional vector occurring from PCA does not have a positive effect on detector performance. In the case of the unprocessed input vector, the sensor grid density influences both POD and FAR, with denser grids yielding better performance, which falls in line with intuitive expectations. It is also noted that the Discordant Outlier method yields very low FAR when the input is passed through PCA. As implied by Figure 32, at least the first two principal components are relatively clustered with the healthy state having significantly lower variance. Taking into account the geometrical nature of the Discordant Outlier method, which in this work was modeled around the healthy state data, it is understood that it is less probable to falsely identify a healthy sample as damaged, thus FAR remains decreased.

It is noteworthy that the ANN can outperform the rest of the methods in the cases with the least available information. This is considered a big advantage of ANNs, since a real-world application would, most likely, collect limited data. In the present work, the employed ANN architecture was rather simple and was based on similar architecture proposed for binary classification in the literature [31]. Exploring the space of the potential architectures in a more formal way, as proposed in works such as that of Alparslan et al [43], would perhaps yield an ANN with better performance. Yet, ANN optimization lies beyond the scope of this analysis.

It is also observed that while the input information increases, the classic statistical methods appear to output a robust performance. This could be attributed to the fact that increasing the available data allows for a better characterisation of the underlying statistical structure of the problem, in terms of the assumed distribution models, hence achieving significantly better performance.

#### **5.4 Detection of localised corrosion**

The detectors were also tested on the ability to detect uniform corrosion over a limited area on the plate. Simulations for this scenario were limited to the 3x3 sensor grid, provided that is the worst

case in terms of information gathering, and to a single damage extent – the 3x3-element damaged area as described in section 3.4 which accounts 0.36% of the entire domain.

The POD and FAR are plotted against thickness wastage, comparing between the detectors. In the localised damage scenario, when submitting the input data to PCA keeping only the first two principal components, the required information is lost resulting in low detection performance across all methods. Nonetheless, when submitting the entire feature vector to analysis, the performance is high, as depicted in Figure 35.

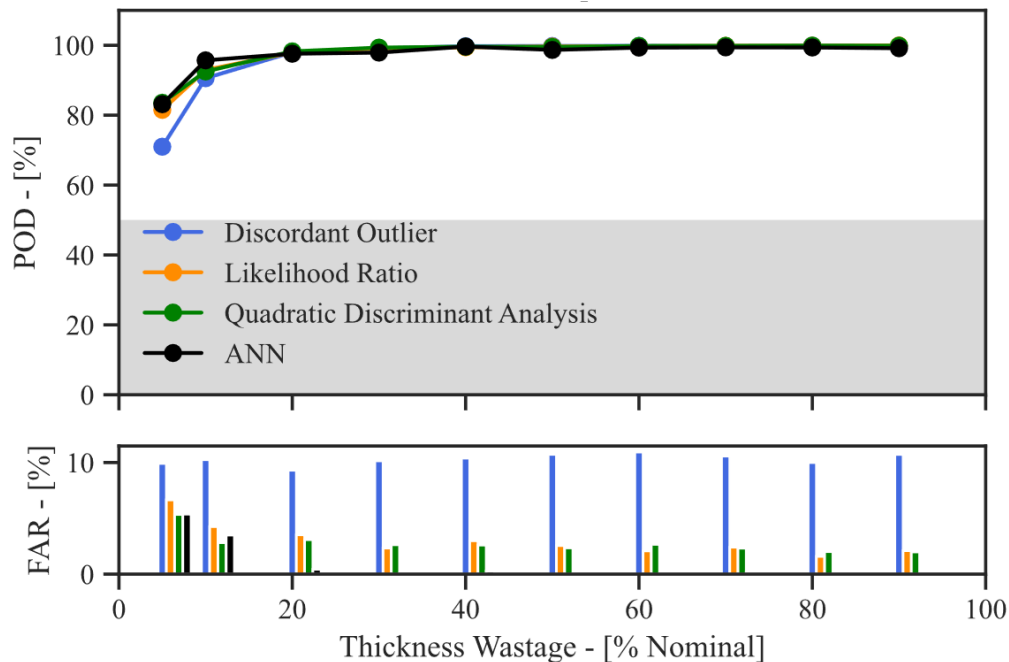


*Figure 35. POD and FAR against thickness wastage percentage in the case of the localised corrosion. Entire feature vector used as input.*

The ability to identify thickness loss of as low as 10% contained within an area as small as 0.36% of the entire domain with a POD above 90% and FAR below 5% is very promising. Regulations require replacement of steel plates where approximately 20% of the nominal thickness is lost. Consequently, being able to identify the existence of locally contained damage at half the replacement threshold, would provide invaluable insight on the condition of the structure. Such information could also be used as a metric to free operational procedures of planned maintenance schemes and pave the way to conditioned based maintenance approaches.



It is important to note that the ability to detect both global and localised corrosion implies that more than one modes of damage can be detected using the same measurements. This raises optimism around the viability of such monitoring solutions, as the acquired data are not strictly problem specific and could be exploited for extracting useful information for various applications.

In the localised damage case, all detectors score very high POD even at the lowest damage severities. It is observed that the ANN marks the least FAR, reaching below 1% by the 20% thickness wastage level. Due to the modeling followed in this study, detection performance is greater in the localised rather than the global damage case. In an effort to explain this behaviour, it is believed that due to the high variability in the loading scenarios, certain combinations of loads and thickness wastage levels can generate similar strain response patterns. Consequently, there is some trade-off between load variability and sensitivity to thickness wastage, which affects the performance of the detectors. On the contrary, when the damage is contained in a limited area on the plate, the disturbance in the strain field is distinguishable regardless of the loading condition. In Figure 36 the strain difference between the healthy plate and a plate with localised damage present for the same loading scenario is visually depicted. This kind of localised disturbance creates a distinct feature in the measurements, increasing the performance of the detectors.

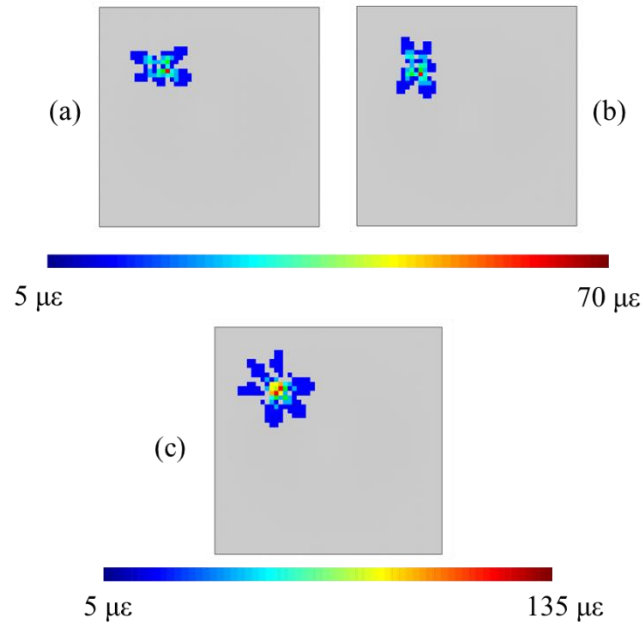


*Figure 36. Disturbance in the strain field on the plate from the existence of localised damage in the (a) normal strain along  $x$  axis, (b) normal strain along  $y$  axis and (c) shear strain on the  $xy$  plane. The grey elements represent the area where there is zero, or near-zero strain difference between the healthy and the damaged plate.*

## 6 Concluding Remarks

### 6.1 General Remarks and Future Research

In the present study, binary damage detection performance in plate-like structures under significant loading variability was investigated. Different SPR methods were considered as part of an SHM system for a rectangular plate under probabilistic loading conditions. Their ability to detect the presence of global and localised damage on the plate using strain measurements as input was assessed. Four sensor arrangements at different densities and three different input vectors were considered. POD and FAR were selected for quantifying the performance of the detectors. The key findings of the employed research are listed below:

- As a result of the modeling of the problem, the performance was higher in localised damage and significantly lower in global uniform corrosion.
- All detectors show promising results in localised damage detection and the ANN also scores the lowest FAR.
- PCA is not the optimal dimensionality reduction approach for the present problem.
- The statistics-based detectors achieve great discrimination performance as the input data dimension increases.
- The ANN can outperform statistics-based detectors in cases with the least available information.

The performance in localised damage detection on this simplified structural domain under high operational variability encourages the investigation of the applicability of a similar SHM paradigm on more complex structural assemblies which could be a solid basis for future work. Additionally, formal modeling of the operational variability, perhaps based on measurements on real structures could be introduced. Finally, towards exploring the viability of such installations by extending their operational utilities, an analysis for additional useful information hidden in the measured data, or alternative useful measurements from the same sensory system for other applications could be conducted.

## 7 Appendix

### 7.1 List of Figures

Figure 1. Sketch of traverse bulkhead with instructions for damage inspection as recommended by IACS guidelines (Source: IACS [1]). .....	2
Figure 2. Flowchart overview of the processes of SHM (Source: Farrar et al [5]). .....	7
Figure 3. Schematic overview of the present work.....	10
Figure 4. Decision boundary visualisation for QDA and LDA on different generic datasets. Comparison between the two variants in different data scenarios. (Source: Scikit-learn [25] (edited)).....	17
Figure 5. Visual representation of the direction of two PCs on bivariate gaussian data. (Source: Wikipedia [29]).....	19
Figure 6. Schematic representation of multilayered feed-forward ANN for binary classification. ....	21
Figure 7. Schematic representation of an artificial neuron. ....	21
Figure 8. Indicative unit step function plot. ....	23
Figure 9. Indicative hyperbolic tangent function plot.....	23
Figure 10. Indicative sigmoid function plot.....	24
Figure 11. Indicative ReLU function plot.....	25
Figure 12. Visualisation of an indicative successful loss minimisation path on a loss surface via SGD. (Source: [33](edited)).....	27
Figure 13. Example of discretisation of a 2D structural frame into a FE model consisting of nine elements and 6 nodes. (Source: [34]).....	29
Figure 14. Example of FE modelling of a T joint between two thin-walled plates. (Source: [35]) .....	30
Figure 15. Example of gap forming between the edges of triangular elements in the distorted state. Case of modeling a beam cantilever with triangular shell elements. (Source: [36]).....	31
Figure 16. Visual explanation of elemental equilibrium and nodal equilibrium on an indicative FE mesh. (Source: [36]).....	32
Figure 17. Modeling of a flat "shell" element by superimposing a "bending" and a "plane stress" element. (Source [36]). .....	35
Figure 18. Typical structural arrangement of a ship's hull bottom. (Source: [38]) .....	38

Figure 19. Top view of the plate with a two-dimensional representation of an instance of the load on it. ....	40
Figure 20. 3D representation of an indicative realisation of the load profile. ....	40
Figure 21. Visual representation of realisations of the load location. ....	41
Figure 22. Sensor topology overview. Each sensor measures longitudinal strain components along x and y axis as well as the in-plane shear strain on the plate. ....	42
Figure 23. Mean and standard deviation of relative absolute differences between measurements plotted against element size as a percentage of the finest element. ....	45
Figure 24. Coefficient of Variation (CV) of relative absolute differences between measurements plotted against element size as a percentage of the finest element. ....	45
Figure 25. Meshed plate and contour plot of the longitudinal ( $\epsilon_x$ ) strain component on the face of the plate for an indicative pressure load realisation. ....	46
Figure 26. Distribution of differences, in absolute strain units, between mean strain features of two feature vectors. ....	49
Figure 27. Indicative probability plots for (a) the healthy state, (b) damaged state and (c) comparative histograms between strain components at healthy and damaged state at corresponding sensor locations. ....	52
Figure 28. Scatterplot matrix of the strains at Sensor 1 (3x3 grid, upper left corner). ....	53
Figure 29. Scatterplot matrix of the strains at Sensor 2 (3x3 grid, middle-top). ....	54
Figure 30. Scatterplot matrix of the strains at Sensor 5 (3x3 grid, central). ....	55
Figure 31. Explained variation retained in each principal component of a vector composed of one healthy and a damaged case in all sensor grid scenarios. ....	56
Figure 32. Comparative pairplot of the first two principal components of healthy and damaged 50% nominal thickness) cases using the 6x6 sensor grid. ....	57
Figure 33. POD and FAR plot against thickness wastage percentage for different input vector cases and regarding (a) Discordant Outlier Analysis, (b) Likelihood Ratio Test, (c) Quadratic Discriminant Analysis and (d) ANN. ....	62
Figure 34. POD and FAR plot against thickness wastage percentage for different input vector cases and sensor grid cases. ....	63
Figure 35. POD and FAR against thickness wastage percentage in the case of the localised corrosion. Entire feature vector used as input. ....	65

Figure 36. Disturbance in the strain field on the plate from the existence of localised damage in the (a) normal strain along x axis, (b) normal strain along y axis and (c) shear strain on the xy plane. The grey elements represent the area where there is zero, or near-zero strain difference between the healthy and the damaged plate..... 67

## 8 References

- [1] International Association of Classification Societies (IACS), "Rec76 - IACS Guidelines for Surveys, Assessment and Repair of Hull Structure - Bulk Carriers," 1994. [Online]. Available: <https://iacs.org.uk/publications/recommendations/61-80/>.
- [2] International Association of Classification Societies (IACS), "Common Structural Rules for Double Hull Oil Tankers and Bulk Carriers," 2022. [Online]. Available: <https://iacs.org.uk/publications/common-structural-rules/csr-for-bulk-carriers-and-oil-tankers/>.
- [3] D. Pantelis and D. Tsiourva, Διάβρωση Και Προστασία Σε Θαλάσσιες Και Μηχανολογικές Κατασκευές (Ακαδημαϊκές Σημειώσεις) [Corrosion and Protection in Marine and Mechanical Structures (Academic Handouts)], School of Naval Architecture and Marine Engineering, Athens: National Technical University of Athens, 2012.
- [4] American Bureau of Shipping, "Rules for Nondestructive Inspection of Hull Welds," American Bureau of Shipping, Houston, 2002.
- [5] C. R. Farrar, S. W. Doebling and D. A. Nix, "Vibration-based structural damage identification," *Philosophical Transactions of the Royal Society A*, vol. 359, no. 1778, pp. 131-149, 2001.
- [6] D. Balageas, C.-P. Fritzen and A. Güemes, Eds., Structural Health Monitoring, London, UK & Newport Beach, USA: ISTE Ltd., 2006.
- [7] K. Worden and C. R. Farrar, Structural health Monitoring: A Machine Learning Perspective, Chichester, West Sussex: John Wiley & Sons, Ltd., 2013.
- [8] M. Ibrion, N. Paltrinieri and A. R. Nejad, "On Risk of Digital Twin Implementation in Marine Industry: Learning from Aviation Industry," *Journal of Physics: Conference Series*, 2019.

- [9] K. N. Anyfantis, "An abstract approach toward the structural digital twin of ship hulls: A numerical study applied to a box girder geometry," *Proceedings of the Institution of Mechanical Engineers, Part M: Journal of Engineering for the Maritime Environment.*, vol. 235, no. 3, pp. 718-736, 1 August 2021.
- [10] A. Rytter, "Vibrational Based Inspection of Civil Engineering Structures [Ph.D. Thesis]," Dept. of Building Technology and Structural Engineering, Aalborg University, Aalborg, 1993.
- [11] K. Worden, A. D. Ball and G. R. Tomlinson, "Fault location in a framework structure using neural networks," *Smart Materials and Structures*, vol. 2, pp. 189-200, 1993.
- [12] H. Sohn, C. R. Farrar, N. F. Hunter and K. Worden, "Structural Health Monitoring Using Statistical Pattern Recognition Techniques," *Journal of Dynamic Systems, Measurement, and Control*, vol. 123, no. 4, pp. 706-711, 2001.
- [13] J. N. Kudva, N. Munir and P. W. Tan, "Damage detection in smart structures using neural networks and finite-element analyses," *Smart Materials and Structures*, vol. 1, pp. 108-112, 1992.
- [14] N. E. Sillionis and K. N. Anyfantis, "Static strain-based identification of extensive damages in thin-walled structures," *Structural Health Monitoring*, 14 October 2021.
- [15] T. Liangou, A. Katsoudas, N. Sillionis and K. Anyfantis, "Statistical Pattern Recognition for Optimal Sensor Placement in Damage Detection Applications," *European Workshop on Structural Health Monitoring*, vol. 2, 2022.
- [16] Y. Yao, Y. Yang, Y. Wang and X. Zhao, "Artificial intelligence-based hull structural plate corrosion damage detection and recognition using convolutional neural network," *Applied Ocean Research*, vol. 90, 2019.
- [17] N. E. Sillionis and K. N. Anyfantis, "On the Detection of Thickness Loss in Ship Hull Structures Through Strain Sensing," *European Workshop on Structural Health Monitoring*, vol. 2, 2022.



- [18] A. Kefal and E. Oterkus, "Displacement and stress monitoring of a chemical tanker based on inverse finite element method," *Ocean Engineering*, vol. 112, pp. 33-46, 2015.
- [19] F. Falcatelli, N. Yue, R. D. Sante and D. Zarouchas, "Probability of detection, localization, and sizing: The evolution of reliability metrics in Structural Health Monitoring," *Structural Health Monitoring*, vol. 0(0), pp. 1-28, 27 December 2021.
- [20] M. Martinez-Luengo, A. Kolios and L. Wang, "Structural health monitoring of offshore wind turbines: A review through the Statistical Pattern Recognition Paradigm," *Renewable and Sustainable Energy Reviews*, vol. 64, pp. 91-105, 2016.
- [21] C. M. Bishop, *Pattern Recognition and Machine Learning*, Cambridge CB3 0FB, UK: Springer Science+Business Media, LLC, 2006.
- [22] S. M. Kay, *Fundamentals of Statistical Signal Processing: Detection theory*, Prentice-Hall PTR, 1998.
- [23] H. Pishro-Nik, *Introduction to Probability, Statistics, and Random Processes*, Kappa Research, LLC, 2014.
- [24] scikit-learn developers, "1.2. Linear and Quadratic Discriminant Analysis," [Online]. Available: [https://scikit-learn.org/stable/modules/lda\\_qda.html#id4](https://scikit-learn.org/stable/modules/lda_qda.html#id4). [Accessed 2022].
- [25] scikit-learn developers, "Linear and Quadratic Discriminant Analysis with covariance ellipsoid," [Online]. Available: [https://scikit-learn.org/stable/auto\\_examples/classification/plot\\_lda\\_qda.html](https://scikit-learn.org/stable/auto_examples/classification/plot_lda_qda.html). [Accessed 2022].
- [26] K. P. Murphy, *Machine Learning: A Probabilistic Perspective (Adaptive Computation and Machine Learning series)*, The MIT Press, 2012.
- [27] I. Jolliffe, "Principal Component Analysis," *Encyclopedia of Statistics in Behavioral Science*, vol. 3, pp. 1580-1584, 2005.
- [28] S. L. Brunton and J. N. Kutz, *Data-Driven Science and Engineering*, Cambridge CB2 8BS: Cambridge University Press, 2019.

- [29] Wikipedia, the free encyclopedia, "Principal component analysis," [Online]. Available: [https://en.wikipedia.org/wiki/Principal\\_component\\_analysis](https://en.wikipedia.org/wiki/Principal_component_analysis). [Accessed July 2022].
- [30] S. Raschka and V. Mirjalili, Python Machine Learning, 3rd ed., Birmingham B3 2PB, UK: Packt Publishing Ltd. , 2019.
- [31] F. Chollet, Deep Learning with Python, Shelter Island, NY 11964: Manning Publications Co., 2018.
- [32] F. Rosenblatt, "The Perceptron - A perceiving and recognizing automaton," Cornell Aeronautical Laboratory, Inc. , 1957.
- [33] M. Fuzellier, "Neural Networks | Fundamentals," 2019. [Online]. Available: <https://towardsdatascience.com/neural-networks-fundamentals-1b4c46e7dbfe>. [Accessed 2022].
- [34] D. Souza, S. L. M. R. Filho, A. L. C. d. Carvalho and N. S. Silva, "Topological Optimization and Genetic Algorithms Used in a Wheel Project for a Drone," *International Journal of Statistics and Applications*, pp. 155-161, 2013.
- [35] IDEA StatiCa, "CBFEM Weld Model: Validation and Verification," IDEA StatiCa, [Online]. Available: <https://www.ideastatica.com/support-center/cbfem-weld-model-validation-and-verification>. [Accessed 2022].
- [36] P. A. Caridis, Finite Element Method and Applications on thin-walled structures (Accademic Handouts) - Υπολογιστικές Μέθοδοι και Εφαρμογές σε Λεπτότοιχες Κατασκευές (Ακαδημαϊκές Σημειώσεις), School of Naval Architecture and Marine Engineering, National Technical University of Athens..
- [37] O. C. Zienkiewicz and R. L. Taylor, The Finite Element Method for Solid and Structural Mechanics, Elsevier, 2005.
- [38] K. N. Anyfantis, Στατική Ναυπηγικών Κατασκευών (Πανεπιστημιακές Σημειώσεις) [Static Structural Mechanics of Marine Structures [Accademic Handouts]] - School of Naval

- Architecture and Marine Engineering - National Technical University of Athens, Athens, 2020.
- [39] V. Papadopoulos and D. G. Giobanis, *Stochastic Finite Element Methods - An Introduction*, Springer International Publishing AG, 2018.
- [40] S. Timoshenko and S. Woinowsky-Krieger, *THEORY OF PLATES AND SHELLS*, McGraw-Hill, Inc, 1959.
- [41] X. Huang, L. Wu and Y. Ye, "A Review on Dimensionality Reduction Techniques," *International Journal of Pattern Recognition and Artificial Intelligence*, vol. 33, no. 10, 2018.
- [42] F. Pedregosa, G. Varoquaux, A. Gramfort, V. Michel, B. Thirion, O. Grisel, M. Blondel, P. Prettenhofer, R. Weiss, V. Dubourg, J. Vanderplas, A. Passos, D. Cournapeau, M. Brucher, M. Perrot and É. Duchesnay, "Scikit-learn: Machine Learning in Python," *Journal of Machine Learning Research*, vol. 12, no. 2011, pp. 2825-2830, 2011.
- [43] Y. Alparslan, E. J. Moyer, I. M. Isozaki, D. Schwartz, A. Dunlop, S. Dave and E. Kim, "Towards Searching Efficient and Accurate Neural Network Architectures in Binary Classification Problems," *2021 International Joint Conference on Neural Networks (IJCNN)*, pp. 1-8, 2021.
- [44] G. P. Zhang, "Neural Networks for Classification: A Survey," *IEEE TRANSACTIONS ON SYSTEMS, MAN, AND CYBERNETICS - PART C: APPLICATIONS AND REVIEWS*, VOL. 30, NO. 4, pp. 451-462, November 2000.
- [45] P. Jeatrakul and K. Wong, "Comparing the Performance of Different Neural Networks for Binary Classification Problems," *2009 Eighth International Symposium on Natural Language Processing*, pp. 111-115, 2009.
- [46] D. Godoy, "Understanding binary cross-entropy / log loss: a visual explanation," *Towards Data Science Inc.*, 21 November 2018.

- [47] B. Ghogh and M. Crowley, "Linear and Quadratic Discriminant Analysis: Tutorial," 2019.
- [48] V. Bushaev, "Understanding RMSprop — faster neural network learning," *Towards Data Science Inc.*, 2 September 2018.
- [49] N. Sillionis, "Diploma Thesis: Damage Identification in Thin-Walled Girders through a Finite Element-Based Digital Twin," Athens, 2020.